Frequency Scanned Interferometry (FSI)

The basis of a survey system for the ATLAS ID using fast automated remote interferometry

A.F. Fox-Murphy,
D.F. Howell,
R.B. Nickerson,
A.R. Weidberg.

University of Oxford, U.K.

1 Introduction

In order to bridge the gap between the expected assembly precision of the ATLAS Inner Detector and the required spacial resolution, it will be necessary to determine the positions of detector elements to high precision after assembly. Traditionally this has been achieved by software analysis of tracking data. Such analyses are lengthy and rely upon an assumption of positional stability of the detector elements over a relatively long period of time. In the ATLAS Inner Detector however, such an assumption may be invalid for a number of reasons. This has prompted the investigation of techniques for directly surveying the Inner Detector during operation. One way to make such direct measurements is to use an interferometric survey system such as the one presented here.

The survey is based around many simultaneous interferometric 1D measurements of absolute length. These measurements will then be combined into a highly overconstrained, 3D geodetic grid and the positions of the individual nodes computed. The Inner Detector will be instrumented with a large number of novel, very low mass interferometers, which will have no moving parts or active components and will require minimal pre-alignment. The interferometers will be remotely illuminated and the resulting interference patterns remotely detected via pairs of single mode optical fibres, possibly several hundred metres long. The actual length determination will be made by counting interference fringes whilst scanning the laser frequency, i.e. by Frequency Scanned Interferometry (FSI). The individual interferometers are each expected to be capable of measuring an absolute distance of about one metre to a precision of a few microns.

The complete survey system is outlined here and the underlying measurement technique, FSI, is described in detail. Preliminary findings made with a laboratory demonstration system for FSI are presented. The geodetic grid and the overall ATLAS alignment strategy will be discussed in further ATLAS Notes.

2 A survey system for the ATLAS Inner Detector

WHY SURVEY THE ATLAS INNER DETECTOR DURING OPERATION ?

Traditionally, once an HEP experiment has been assembled, the positions of the tracking elements have been determined by long and labour-intensive software analyses of large quantities of tracking data. Such processes, besides being difficult and laborious, require the assumption that the detector positions were reproducible over the data collection period.

There are a number of reasons why it is possible that the ATLAS Inner Detector will not be stable over the periods of time necessary for the collection of sufficient data for such track-based alignment calculations. One possible cause of significant movements in the silicon subdetector is the dependence of the power dissipation of the front-end electronics on the occupancy levels and trigger rates, and hence on the varying luminosity of the LHC during a run. Overall, the average temperature of the detector should be held constant by the cooling system, but it is possible that the changes in the temperature distributions between the heat sources (front-end chips) and the heat sinks (cooling pipes) will be large enough to cause significant changes in the shape of the silicon subdetector.

Reasons such as these make it attractive to investigate direct, fast, automatic, remote and computationally simple ways of surveying the positions of critical parts of the Inner Detector during operation. The survey system described here is one possible solution.

SPECIFICATIONS FOR THE SURVEY SYSTEM

The essential requirement is for a system capable of producing a 3D map of the positions of strategically chosen parts of the detector in a time short enough for any mechanical or thermal drifts of the detector during that period to be small compared with the measurement precision. The 3D precision with which any one section of the Inner Detector can be related to any other must be below about 10 μm in order to meet the physics specifications. See Table 1 [4][2].

Subdetector	ϕ	r	z
Pixel (barrel)	15 (100)	80 (250)	87 (250)
Pixel (forward)	15 (100)	80 (250)	87 (250)
Si	25 (100)	80 (250)	625 (500)
GaAs	28 (100)	80 (500)	707 (500)
MSGC	45 (200)	160 (1000)	894 (1000)
TRT (barrel)	187 (200)	1200 (1000)	1000 (1000)
TRT (forward)	187 (200)	1200 (1000)	1000 (1000)

Table 1: *The required spacial resolutions and, in brackets, the expected pre-survey assembly precisions.*

Continuous operation is likely to be impossible, so a system is needed which can make absolute measurements of position with no *a priori* knowledge. Many existing metrological techniques are only capable of monitoring variations in position and are therefore ruled out by this requirement.

As for any system used in ATLAS, the intra-detector elements must have low radiation length, very low mass, small physical size, must be radiation hard, must have no moving parts, must require no maintenance or adjustment during operation, and must communicate with the outside world via wires, pipes or fibres.

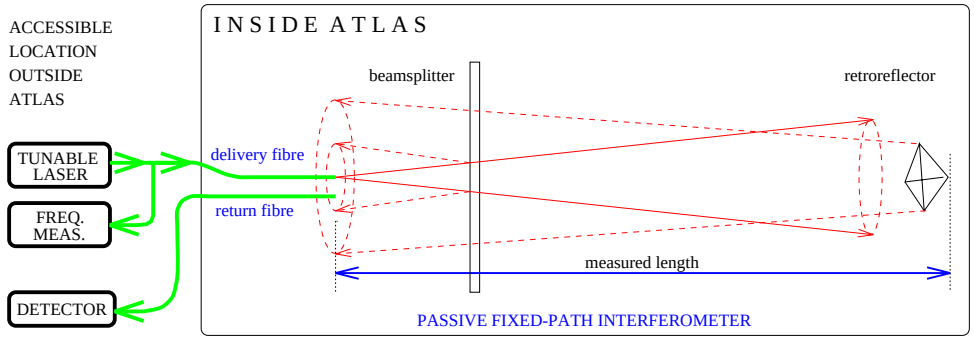

Figure 1: *The basic concept of the FSI system.*

THE PROPOSED SOLUTION

The solution proposed here to satisfy the requirements given above is a system based upon making a large number of simultaneous length measurements between selected points (nodes) in the Inner Detector, each node being common to several such measurements. The nodes are arranged in a highly overconstrained 3D geodetic grid to allow computation of the node positions in three dimensions. A novel automated remote metrological technique, Frequency Scanned Interferometry (FSI), is being developed to make the length measurements. Overall, the Inner Detector survey system may be considered to be the combination of the FSI system, the geodetic grid, temperature and pressure sensors, and quasi-real-time (fast offline) computation.

The FSI system is based upon a novel, very low mass interferometer, in which the illumination and the detection of the interference pattern are both done remotely using a pair of single mode optical fibres. One fibre is coupled to a tunable laser located outside the detector. The other is connected to a photodetector, also located externally. The interferometer is designed to be capable of measuring to micron precision elements of a 3D network with a shape unknown at the millimetre level, and to this end employs a retroreflector (see Section 3.7). This minimises the pre-alignment of the optics during assembly of the Inner Detector and ensures that no adjustment is needed during operation or normal maintenance cycles. In each interferometer, the measured distance is between a known point near the closely positioned ends of the fibre pair and the corner-point of a retroreflector mounted some distance away. A single interferometer design is capable of making measurements in the range $\sim$10 cm to $\sim$1.5 m.

The measurement is made by scanning the optical frequency of the laser and calculating the ratio of the change in frequency to the number of fringe oscillations seen at the photomultiplier. By using optical splitters many interferometers can be served simultaneously by one tunable laser and one frequency measurement system. All of this is located outside the detector (probably in the counting room) and is the same regardless of the number of measurements made. Since these external optical systems are the major cost in the FSI system, the incremental cost of additional measurements is comparatively low, which makes FSI a suitable choice for the present application in which many (possibly several hundred) simultaneous length measurements will be required.

In order to meet the specification of a 3D precision of 10 μm, the 1D precision must be of the order of 1 μm to take account of the errors associated with the positioning of the measurement endpoints and the triangulation. The possibility that within the detector there could be mechanical vibrations with an amplitude greater than $\frac{\lambda}{2}$ has led to the

investigation of a data acquisition technique which should be capable of both rejecting and analysing the vibrations.

It is important to note that the desired quantities, namely spatial positions, are measured directly, with no coupling of other variables such as the (non-uniform) B-field. This means that there are no intrinsically preferred directions, which is not the case with track-based alignment techniques.

The control system, the data acquisition and the metrological and geometrical analyses will be automated to provide a continuous quasi-real-time survey of the detector with minimal human intervention. Since it makes absolute measurements of distance, the system may be powered down at any time without penalty.

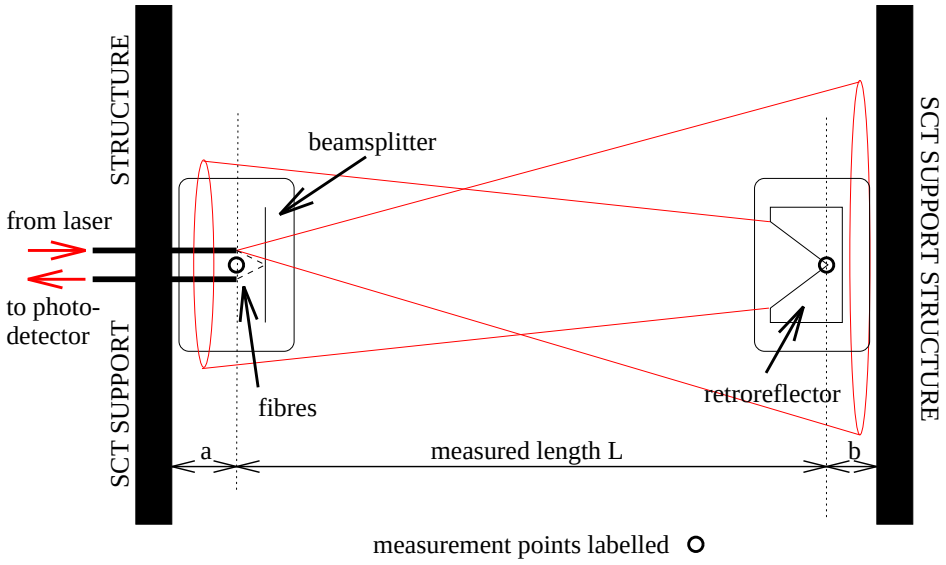

Figure 2: *A measurement is made between two sections of the SCT support structure. Part of the diverging laser beam is reflected back towards the return fibre by a corner-cube retroreflector. A glass sliver placed in the beam acts as a weak beamsplitter to return a small fraction directly to the return fibre. The fundamental measurement is made between the point midway between the two fibres and the corner-point of the corner-cube. Corrections are applied to relate it to points on the support structure: the pathlength of the reference beam is measured in a laboratory calibration and the lengths such as* a *and* b *are measured during assembly.*

3 Frequency Scanned Interferometry

3.1 Introduction

In any interferometer a light beam is divided into two or more parts which travel along different paths and subsequently recombine to form an interference pattern. The form of the interference at any point in the pattern is determined by the vector sum of the electric fields at that point, and so depends on the amplitudes and phases of the electric fields in each of the interfering beams.

If there are just two beams then the combined intensity $I(\mathbf{r})$ at a point $\mathbf{r}$ is given by

$$I(\mathbf{r}) = I_1 + I_2 + 2\sqrt{I_1 I_2}\cos(\phi_1(\mathbf{r}) - \phi_2(\mathbf{r})) \tag{1}$$

where I_1 and I_2 are the individual intensities of the two beams, and $\phi_1(\mathbf{r})$ and $\phi_2(\mathbf{r})$ are the spatial parts of the phases of the two electric fields.

With no loss of generality, the phases of both beams may be taken as zero at the point where they are split from one common beam. The total change in the phase of the electric field over the path of beam i is proportional to the 'optical path' $\mathcal{D}_i$ (the equivalent path length *in vacuo*), which may be expressed as

$$\mathcal{D}_i = \sum_{\text{subpaths } j} n_{ij} l_{ij} = \overline{n}_i L_i \quad i = 1, 2 \tag{2}$$

where n_{ij} is the refractive index for each section of the path, l_{ij} is the geometric length of each section, $\overline{n}_i$ is the overall path-averaged refractive index, and L_i is the total geometric path length.

The phase difference in Equation 1 may now be written as

$$\Phi \equiv \phi_1 - \phi_2 = 2\pi(\mathcal{D}_1 - \mathcal{D}_2)\frac{\nu}{c} \tag{3}$$

where $\mathcal{D}_1$ and $\mathcal{D}_2$ are the optical paths of the two beams, ν is the optical frequency of the light, and c is the speed of light. Thus the combined intensity depends on the 'optical path difference' (OPD) and on the optical frequency of the light [1].

The phase terms at the heart of the description of any interferometer have the same form, namely

$$\text{phase} \propto (\text{length}_1 * \text{index}_1 - \text{length}_2 * \text{index}_2) * \text{frequency} \tag{4}$$

By looking at the the manner in which the interference pattern varies as one of the five quantities in the above equation is changed, one may obtain information about any one of the other four provided that the other three are known. Clearly there are three physical quantities which are measurable with an interferometer (either singly or in combination) : length, refractive index and frequency. Commonly it is either the geometric length or the refractive index of one of the paths (arms) which is varied, with the optical frequency remaining constant. If an interferometer is not permitted to have any moving parts and all the refractive indices are constant, i.e. the optical paths are fixed, then the only remaining variable is the optical frequency.

In the past, a commonly used technique for obtaining length measurements from a fixed-path interferometer was to record the detected intensity for a number of different

[1] Since the wavelength of light changes depending on the refractive index of the medium in which it is travelling, it is more convenient to talk in terms of optical frequency since it is invariant in this respect.

wavelengths and to solve the resulting set of simultaneous equations using the *method of exact fractions* [8][9]. The use of such a technique, known as 'multiple discrete wavelength interferometry', requires some *a priori* knowledge of the length which is to be measured, and is not suitable for the simultaneous measurement of many widely different lengths since the choice of wavelengths depends to some extent on the lengths to be measured.

Recent advances in tunable laser technology have made it feasible to consider the simultaneous, absolute measurement of many different lengths with no such prior knowledge. If the optical frequency in a fixed-path interferometer is varied (scanned) continuously over the range $\Delta\nu$, then the phase Φ also varies continuously, resulting in oscillations in the combined intensity I, with the number ΔN of oscillations or 'fringes' being given by

$$\Delta N = \frac{\Delta\Phi}{2\pi} = \frac{\Delta\nu}{c} \mid \mathcal{D}_1 - \mathcal{D}_2 \mid \tag{5}$$

$$= \frac{\Delta\nu}{c} \mid \overline{n}_1 L_1 - \overline{n}_2 L_2 \mid \tag{6}$$

where ΔN is not necessarily an integer.

In order to extract one of the the geometric paths L_1, it is necessary to know the values of $\overline{n}_1$ and $\overline{n}_2 L_2$. Then the measured length is given by

$$L_1 = \frac{1}{\overline{n}_1}\left(\frac{c\Delta N}{\Delta\nu} + \overline{n}_2 L_2\right) \tag{7}$$

If the interferometer is constructed in such a way as to make the reference path L_2 stable *by design* then L_2 need only be determined once by means of a calibration measurement. The required stability may be achieved by choosing L_2 to be much shorter than L_1 so that for mechanical or thermal changes $\frac{\Delta L_2}{L_2}$ is much less than $\frac{\Delta L_1}{L_1}$. This also reduces the sensitivity to changes in $\overline{n}_2$. If the error on $\overline{n}_2 L_2$ is negligible then the precision of the measurement of L_1 is given by

$$\frac{\sigma_{L_1}}{L_1} = \sqrt{\left(\frac{\sigma_{\Delta N}}{\Delta N}\right)^2 + \left(\frac{\sigma_{\Delta\nu}}{\Delta\nu}\right)^2 + \left(\frac{\sigma_{\overline{n}_1}}{\overline{n}_1}\right)^2} \tag{8}$$

where σ_{L_1}, $\sigma_{\Delta N}$, $\sigma_{\Delta\nu}$ and σ_{n_1} are the measurement errors of L_1, ΔN, $\Delta\nu$ and $\overline{n}_1$ respectively.

It should be noted that multiple lengths may be measured simultaneously by using light from a single laser to illuminate multiple interferometers and recording the detected fringe intensity for each one concurrently. If the the phase measurement accuracy $\sigma_{\Delta N}$ and the required length precision σ_{L_1} are both independent of the length measured, then a single frequency sweep $\Delta\nu$ is suitable for all the interferometers.

Thus the geometric path lengths of one of the arms of each of a set of fixed-path two-beam interferometers may be determined simultaneously by scanning the optical frequency of a single laser and recording the fringes seen at a set of detectors. This is the basic principle behind FSI. The next step is to design an interferometer in which the measured geometric path length L_1 is related in a simple way to a desired length (R say), and to examine whether the required accuracy can be attained, whilst satisfying the constraints imposed by the use of such a technique within ATLAS.

3.2 Interferometer design

Since the structure to be measured will be inaccessible and in a hostile environment, it will not be possible to place a laser source, photodetectors or any moving parts inside the detector. The only viable method of constructing interferometers in such conditions is to use optical fibres for the delivery and reception of light. Each interferometer is therefore connected to a pair of radiation hard fibres (single mode for reasons explained below). The laser is coupled into one fibre of each pair, using a series of splitters, whilst the second fibre of each pair returns light from the interferometer to a small photomultiplier or avalanche photodiode. The fibres may be several hundred metres long, meaning that all the complex optics may be accessible and in a non-hostile environment.

Figures 1 and 2 illustrate schematically the interferometer design which is proposed for use in ATLAS. The measurement is made between two accurately known points on two millimetre-sized objects precisely positioned within the Inner Detector. The first is a mounting block in which the two fibres are fixed parallel to each other a short distance apart with a small sliver of glass mounted in front them to act as a beamsplitter. The second object is a retroreflector (see Section 3.7) mounted some distance away on another part of the structure.

There are no lenses in front of the fibres, so the beam emitted from the delivery fibre is conical, as is the acceptance region of the return fibre. The intensity distribution within the laser cone is gaussian with a usable width of about $\pm 3^{\circ}$ and a sharp cutoff at about $\pm 5^{\circ}$. See Appendix D for details of the coupling properties of single mode fibres.

A small fraction of the light emitted from the delivery fibre is reflected directly into the return fibre by the beamsplitter. Most of the light in the laser cone passes through the beamsplitter towards the retroreflector. The retroreflector returns a fraction of this forward-going light cone back towards the fibres, of which a fraction is coupled into the return fibre. Thus there are two paths within the interferometer and hence two interfering beams incident on the return fibre. Detailed calculations of the optical path lengths are given in Appendix A.

It is essential that both optical fibres are monomode. The phase relationship between the different modes of a multimode fibre is not constant, depending strongly on the temperature and mechanical state of the fibre. For this reason, a multimode laser delivery fibre would result in a light field with insufficient spatial coherence. Use of a monomode delivery fibre ensures that there is a constant phase relationship between the light at all points within the interferometer independent of the state of the delivery fibre. Similarly, the return fibre must be monomode. It can be shown that, using a monomode return fibre, the intensity at the photodetector is simply proportional to the intensity at the centre of its input face (see Appendices A and D). Thus the use of monomode fibres ensures that the measured optical path difference is intrinsically independent of the fibres.

The optical efficiency of the interferometer is calculated in Appendix C. If photomultipliers or avalanche photodiodes are used to detect the interferometer fringe signals then the required fringe phase accuracy should be attained with an input optical power of around 10 mW for each interferometer.

It is possible that there may be vibrations of the Inner Detector support structure with an amplitude greater than $\frac{\lambda}{2}$. Immunity to such vibrations can be achieved by utilising a technique known as phase-shift interferometry (PSI). This is explained in detail in Appendix B. An acousto-optic modulator is used to produce a small, rapid dithering of the laser frequency (in addition to the long, slow, monotonic FSI frequency sweep). Provided

that the modulation is performed at a sufficient rate (determined by the maximum vibratory velocity), the phase of the fringe pattern may be determined directly for each point in the FSI scan, which allows analysis and hence rejection of the vibration. See Figure 3.

It is essential to examine the geometry of the interferometer in detail in order to find out precisely how the measured optical path length is related to the desired length. It is shown in Appendix A that if R_c is the radial distance from the point midway between the fibres to the corner-point of the corner-cube, n_g is the refractive index of the gas near the beamsplitter, $\overline{n}_g$ is the path averaged refractive index of the gas, n_b is the refractive index of the beamsplitter material and d is the thickness of the beamsplitter, then

$$\mathcal{D}_1 = 2\left(\overline{n}_g R_c + d\left[\frac{n_b}{\cos\theta_2} - \frac{n_g}{\cos\theta_1}\right]\right) \tag{9}$$

where θ_1 is the angular position of the corner-cube with respect to the axis defined by the fibres and $n_g \sin\theta_1 = n_b \sin\theta_2$. See Figures 12–15.

Note that Equation 9 contains two angular terms. These terms account for the fraction of the path $\mathcal{D}_1$ which is within the (flat) beamsplitter and so they vary according to the angle of the measurement axis with respect to the axis defined by the fibres. It is likely that the angular position of the corner-cube with respect to the fibres will always be known to within $\pm 1^\circ$ (i.e. within ± 1.7 cm at 1 m distance). If d =1 mm, $n_g = 1.0$ and $n_b = 1.5$, then if the position of the corner-cube is imagined to be swept around the arc R_c =1 m, the fractional variation in the optical path $\mathcal{D}_1$ may be expressed as

$$\frac{\mathcal{D}_1(\theta_1 = 0) - \mathcal{D}_1(\theta_1 = 1^\circ)}{\mathcal{D}_1(\theta_1 = 0)} = 1.6 \times 10^{-7}$$

This ratio rises to 4.6×10^{-7} for $\sigma_{\theta_1} = 3^\circ$. The beamsplitter thickness d will in fact be much less than 1 mm and so the small angular effect may be ignored, giving

$$R_c = \frac{1}{\overline{n}_g}\left[\frac{1}{2}\left(\frac{c\Delta N}{\Delta\nu} + \mathcal{D}_2\right) - d\,(n_b - n_g)\right] \tag{10}$$

The value of $\mathcal{D}_2$ is a constant for each fibre/beamsplitter unit, and will be measured in a laboratory calibration so that each measured length R_c may be related to a set of fiducial marks on the outer faces of the two endpoint blocks. These fiducials will be used as positioning guides during the microscopic assembly of the Inner Detector, with the result that each measured R_c will be related to a distance $R_{\text{structure}}$ between two known points on the support structure, i.e.

$$R_{\text{structure}} = R_c + \text{end corrections} \tag{11}$$

Given that the (constant) end corrections are known, it only requires knowledge of the path-averaged refractive index of the gas to be able to calculate the distance between two sections of support structure from an FSI scan.

3.3 Refractive index

In order to be able to extract spatial dimensions from measurements of optical path lengths in a gaseous medium, the path-averaged refractive index of the gas must be determined.

The refractive index of a gas is a function of temperature and pressure and of the partial pressures of water vapour (humidity), carbon dioxide, and of any other significant gas constituent of the local atmospheric environment which is active at the wavelength used.

A widely used equation [10] for the refractive index of dry air under standard conditions of temperature and pressure (15 °C, 1013.25 mbar) is

$$(n_{std} - 1).10^8 = 8342.13 + \frac{2406030}{130 - \sigma^2} + \frac{15997}{38.9 - \sigma^2} \tag{12}$$

where $\sigma = \frac{1}{\lambda_{vac}}$ is the vacuum wavenumber in $\mu\mathrm{m}^{-1}$. This formula is correct to within 0.01 ppm over the range λ_{vac} =200–1000 nm. The refractive index, n_{TP} at any temperature T °C and pressure P mbar may then be computed from

$$(n_{\mathrm{TP}} - 1) = (n_{std} - 1).\left(\frac{100\,\mathrm{P}[1 + \mathrm{P}(61.3 - \mathrm{T})10^{-8}]}{96095.4(1 + 0.003661\,\mathrm{T})}\right) \tag{13}$$

Further small corrections need to be made for the partial pressures of water vapour and CO_2. From the above equations it can be shown that a change in measured OPD of 0.1 ppm can be induced by an air temperature change of 0.1 °C, or an air pressure change of 0.3 mbar, or a humidity change of 10 % or a CO_2 level change of 600 ppm. The figures for a dry nitrogen environment are very similar. Those for helium are better by about a factor of ten.

A distinction should be made between global temperature variations which affect the overall scale of the measurements (but not the measured 3D shape), and local temperature variations which may affect individual measurements differently. Pressure variations will be global, at least within each subdetector.

The path-averaging means that even quite large local temperature changes are not serious provided that the path lengths through them are small compared with the total path lengths. It takes an uncertainty of 3 °C over the whole length of a 30 cm measurement to generate a 1 μm error.

Temperature sensors isolated from the structure will be used to measure the gas temperature at selected points within the Inner Detector. It remains to be seen how much convection- and flow-induced mixing there will be in the Inner Detector.

It may be possible to distinguish large local gas temperature changes from real movements using the 3D geometric analysis. If localised heating around a grid node results in a sufficiently large change in the set of FSI measurements associated with that node, the analysis software may be unable to treat it as being due to single motion and so may be able to flag it as resulting from a refractive index change.

Atmospheric turbulence causes variations of density and hence a fluctuating refractive index, so the analysis and rejection of turbulence is similar to the treatment of mechanical vibration which is described in Appendix B.

3.4 The frequency scan

In order to meet the specification of a 3D precision of $10\,\mu$m, the 1D precision must be of the order of $1\,\mu$m to take account of the errors associated with the positioning of the measurement endpoints and the triangulation. From Equation 8 it can be seen that the precision σ_{R_c} of the length measurement extracted from an FSI scan is a function of the fractional errors of the measured change in fringe order ΔN and of the measured optical frequency change $\Delta\nu$. The proposed method of direct fringe phase measurement is explained in Appendix B. The optical signal detection is discussed in Appendix C. Assuming that the error on the refractive index is small, the measurement precision is given by

$$\left(\frac{\sigma_{R_c}}{R_c}\right)^2 = \left(\frac{\sigma_{\Delta N}}{\Delta N}\right)^2 + \left(\frac{\sigma_{\Delta\nu}}{\Delta\nu}\right)^2 \tag{14}$$

From Equation 10 it can be seen that if $d, D_2 \ll R_c$ and $n_g \sim 1$

$$\Delta N \sim \frac{2R_c\Delta\nu}{c} \tag{15}$$

Eliminating ΔN from Equation 14, the required frequency sweep $\Delta\nu$ may be expressed as

$$\Delta\nu \simeq \sqrt{A^2 + B^2} \tag{16}$$

$$\text{where} \quad A = \left(\frac{c\sigma_{\Delta N}}{2\sigma_{R_c}}\right) \quad \text{and} \quad B = \left(\frac{R_c\sigma_{\Delta\nu}}{\sigma_{R_c}}\right) \tag{17}$$

If the required measurement precision is $\sigma_{R_c} = 1\,\mu$m, and if the signal-to-noise ratio of the detected fringes is sufficient to be able to determine the phase Φ to within $\frac{2\pi}{100}$ (i.e. $\sigma_{\Delta N} = \frac{1}{100}$), then $A = 1.5\,$THz, independent of R_c. A represents the lowest possible value of $\Delta\nu$ for a given measurement precision and fringe signal-to-noise ratio. For reasons of scan time and laser limitations it is desirable to make the scan as short as possible, and so the value of B should be comparable to or less than A.

From the form of B it can be seen that for a given scan length $\Delta\nu$ the frequency measurement requirement becomes more stringent as R_c increases. If B is required to be similar to or less than A, then for the worst case range $R_c \sim 1\,$m the frequency measurement error $\sigma_{\Delta\nu}$ must of the order of 1.5 MHz.

Thus a reasonable value for the length of the frequency scan $\Delta\nu$ is about 3 THz, giving $\Delta N = 20,000$ for $R_c = 1\,$m.

Tunable lasers are available which will sweep over the required 3 THz, although not continuously : during tuning the optical frequency of most tunable lasers goes through discontinuities due to 'hops' between different cavity modes. A scan must therefore be composed of a number of shorter frequency sweeps (sub-scans) which are then linked together using absolute optical frequency measurements. See Figure 3. The sub-scans must be close enough in frequency to be able to determine exactly the integer number of fringes between one sub-scan and the next by extrapolation of Φ vs. ν. This use of several short sub-scans is anyway highly desirable since it considerably reduces the amount of data collected and hence the time required for the full scan.

The need to combine several short scans necessitates the measurement of absolute laser frequencies and not just relative frequencies. In order to extract relative optical frequency changes $\Delta\nu$ with an accuracy of 1.5 MHz from the difference of two absolute frequency measurements, the precision of the latter must be around 0.75 MHz.

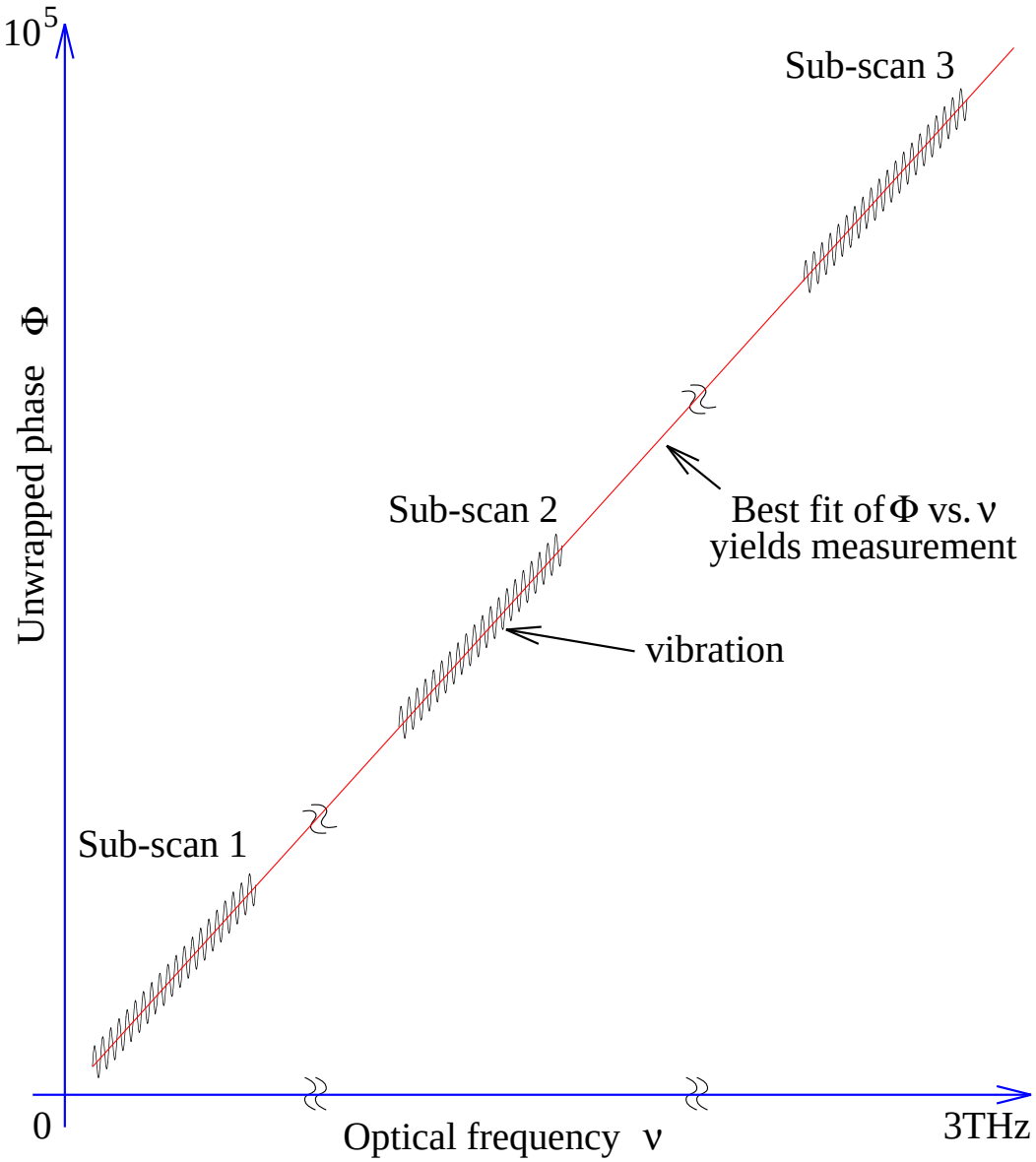

Figure 3: *Several sub-scans are needed to cover the required scan range. If the 'unwrapped phase' Φ (see Appendix B) is plotted against laser frequency ν then the gradient of the best fit line yields the OPD and hence the measured length. A single frequency component vibration is shown, appearing as a sinusoidal deviation from the best fit straight line. For a 1.0 m measured length $\Delta\Phi = 2\pi \times 20,000$ and $\Delta\nu = 3$ THz.*

So, to recap, a reasonable choice of scan parameters is:

$$\begin{array}{rcl@{\qquad}rcl} \Delta\nu & \geq & 3\,\mathrm{THz} & \sigma_{\Delta N} & \leq & \frac{1}{100} \\ \Delta N & \geq & R_c[\mathrm{m}] \times 20,000 & \sigma_\nu & \leq & 0.75\,\mathrm{MHz}/R_c[\mathrm{m}] \end{array}$$

3.5 Tunable laser selection

The choice of laser is determined by the required frequency stability, power, and tuning capability.

The frequency stability must be less than the frequency measurement precision of 0.75 MHz. The optical power required for each individual interferometer is around 10 mW (see Appendix C), so a laser power of the order of 1 W would be suitable. The total tuning range must be greater than 3 THz, with a mode-hop-free tuning range which is as large as possible. If the rate of change of laser wavelength is insufficiently constant then the fringe phase measurement and the ability to measure the wavelength will be degraded. In this context, the most suitable way to tune a laser is by mechanical alteration of the laser cavity length using a piezo-electric actuator locked to a variable reference cavity.

Commercial tunable single frequency Ti:sapphire lasers exist which meet the specifications given above [42][43]. For example, the MBR-110 from Microlase Optical Systems delivers 1 W/2 W optical power when pumped by a 7 W/13 W argon ion laser and is tunable over the range 700–1050 nm. The mode-hop-free tuning range is 30 GHz. The laser cavity is piezo-stabilised to a reference cavity, resulting in a frequency stability better than 100 kHz RMS. A servo-controlled piezo-electric scan provides better than 0.5% scan linearity. The scan is digitally controlled up to 30 GHz, and the scan time can be set digitally from 5–4000 seconds.

Due to considerable commercial pressure, the rate of development of tunable lasers is high. It is likely that the performance and cost will improve before the final laser selection for the ATLAS FSI system has to be made.

3.6 Optical frequency measurement

As explained above, the FSI scan is composed of a number of sub-scans linked together using measurements of absolute optical frequency.

A commonly used technique for measuring the *absolute* optical frequency of a laser is to compare the unknown laser wavelength with that of a known laser using a two-beam interferometer in which the path difference between the two arms is varied periodically, typically by several centimetres several times a second. Then the ratio of the two wavelengths is given by the ratio of the rate of fringe detection for each of the two sources. Such a device is known as a 'wavemeter'. Commonly available wavemeters have a maximum accuracy of about one part in 10^6 and typically give a reading several times per second. Higher precision is possible at the cost of a longer measurement time. The reference laser is typically a frequency-stabilised He-Ne laser integrated with the interferometer in one benchtop unit.

Very precise measurements of *relative* optical frequency may be obtained by using a Fabry-Pérot étalon [9]. This is an interferometric device constructed from two partially reflecting optical flats which are mounted parallel a short distance apart to form an optical cavity. The interference caused by multiple reflections between the inner surfaces results in a transmission pattern which is an infinite set of equally spaced sharp peaks. See Figure 4. The optical frequency spacing between the transmission maxima is known as

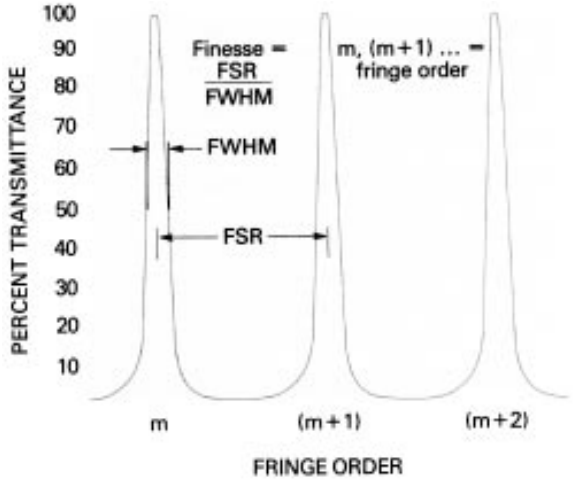

Figure 4: *The transmission pattern of a Fabry-Pérot étalon. The horizontal axis is light frequency, or wavelength, or fringe order number, or time when frequency-scanning. The 'free spectral range' (FSR) of an étalon is the spacing of the transmission peaks, usually quoted in Hz. The 'finesse', $\mathcal{F}$, is a measure of the sharpness of the peaks and is given by $\mathcal{F} = \frac{FSR}{FWHM}$, where FWHM is the 'full width at half maximum' of the peaks.*

the 'free spectral range' (FSR), and is given by FSR= $\frac{c}{2nd\cos\theta}$ where c is the speed of light, d is the width of the gap between the two glass sheets, n is the refractive index of the material in the gap (often air), and θ is the angle of incidence of the laser beam on the étalon. The 'finesse' of an étalon is a measure of the sharpness of the peaks. It is numerically equal to the ratio of the FSR to the 'full width at half maximum' (FWHM) of the peaks. For good quality étalons the finesse is generally of the order of 100.

By recording the intensity of the transmitted beam whilst sweeping the optical frequency, and fitting the logged data to find the positions of the transmission peaks, it is possible to obtain a set of precisely known markers of relative frequency vs. time.

The frequency measurement technique proposed for FSI combines the absolute frequency measurement capability of a wavemeter with the high precision of a set of Fabry-Pérot étalons. Each device is fed with a beam extracted from the main laser beam. The transmitted signals of the étalons are all logged continuously during the scan. The wavemeter is used for a single stationary measurement of frequency at the beginning and/or end of each sub-scan.

The basic idea is to make use of an étalon (E_1) with a free spectral range (FSR) greater than twice the frequency uncertainty of a wavemeter measurement. If one transmission peak of this étalon is arbitrarily taken as order zero and its frequency is measured with the wavemeter then the order of any other peak relative to the zeroth one can be determined with a single wavemeter measurement, provided that the FSR is known accurately. Hence the frequency relationship between sub-scans can be determined by holding the laser frequency constant at one of the E_1 peaks near the beginning or the end of each sub-scan and using the wavemeter to measure its frequency.

A second étalon (E_2) may be used to increase the accuracy and number of the frequency markers within a sub-scan. As for E_1 the transmitted signal is logged continuously during the scan. The FSR of E_2 is chosen to be more than twice the frequency error which arises in fitting the peaks of the logged E_1 trace. If the ratio of the FSRs of E_1 and E_2 is very

stable and is measured independently to high precision, it is possible to use a fitted E_1 peak to determine the order of an E_2 peak relative to an arbitrarily defined zero order peak in a previous sub-scan. The frequency measurement error is then the fitting error for the narrower E_2 peaks. In a similar way a third étalon (E_3) may be used to provide a further improvement in precision and a greater number of frequency markers. It is expected that three étalons will be needed to reach the required precision.

In the system proposed for ATLAS, the étalons will be placed in a temperature controlled and evacuated enclosure to ensure their stability. The longest cavity may be stabilised by actively locking its length to a small reference laser such as a He-Ne laser, itself locked to a saturated absorption feature of an iodine vapour cell. In this way, the ratios of the cavity lengths will be held constant to within 0.05 ppm or better. The FSRs of each of the étalons will be measured optically, and recalibrated whenever necessary.

3.7 Retroreflectors

A retroreflector is a reflecting object which returns a light ray parallel to its incident direction. One of the best known devices of this type is is the 'corner-cube' or 'cube corner retroreflector' [37, 38, 39, 40, 41]. It is based upon three reflecting surfaces arranged as in one corner of a cube. Any light ray hitting the inside surface of such a cube corner will be reflected up to three times and returned parallel to the incident ray. A corner-cube may be either be constructed from three mirrored surfaces, in which case the reflection takes place externally, or it may be a prism such as the one shown in Figure 5, in which case there is total internal reflection. For the purposes of a system intended for use in the ATLAS environment, an externally reflecting corner-cube is preferred. This gives lower optical losses, lower mass, and elimination of any problems which might be associated with loss of transparency due to radiation damage or variation of refractive index with wavelength.

The geometrical properties of the corner-cube retroreflector are discussed in detail in Appendix A where it is shown that the use of retroreflectors in FSI makes the system intrinsically insensitive to the exact relative positions and orientations of the end points of the the measurement. This has a number of important advantages:

- No pre-alignment of the interferometers is necessary, and changes in the shape of the detector have no effect on the performance of the optics.
- More than one measurement can be made simultaneously to a single corner-cube. That is, a corner-cube may be the target of more than one laser light cone. If, conversely, there is more than one corner-cube within a laser light cone, then provided that the lengths are sufficiently different, it may be possible to extract more than one length from a single fringe pattern.
- The above features result in more freedom in the design of the grid nodes since the number of corner-cubes may be less than the number of lengths measured.

3.8 Three-dimensional combination of measurements

A preliminary design for the 3D grid for the SCT Si barrel is shown in Figures 7 and 8. It is intended that several corner-cube reflectors and several fibre/beamsplitter units will be combined in one object to form one node of the 3D grid. A conceptual design for this complex multifacetted object, or 'jewel', is shown in Figure 6. At least two different different jewel designs will be needed to cover the whole grid. Is is hoped that the jewel

may be made of reflection-coated injection-moulded plastic or constructed from silicon. A number of grid layouts and their triangulation performances have been considered in detail in [1, 3, 5, 6].

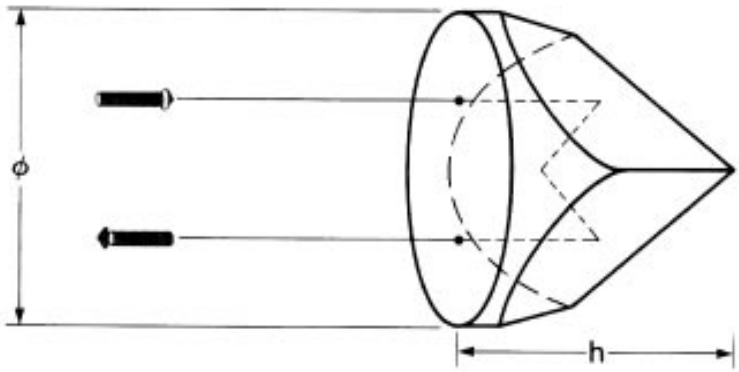

Figure 5: *A prism type corner-cube. The reflecting surfaces are internal. Externally reflecting corner-cubes are preferred for use in the ATLAS environment.*

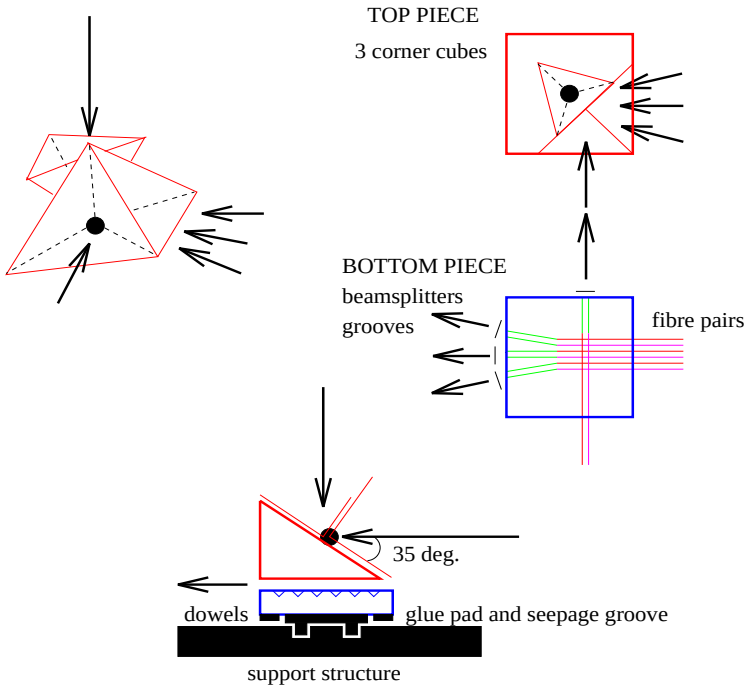

Figure 6: *Conceptual design for a 'jewel'. Three corner-cubes and four fibre/beamsplitter units are combined in a manner appropriate to make one node of the end-plane alignment grid of Figure 7, all nodes being identical. The corner points of the retroreflectors are common, which simplifies the post-scan geometrical analysis.*

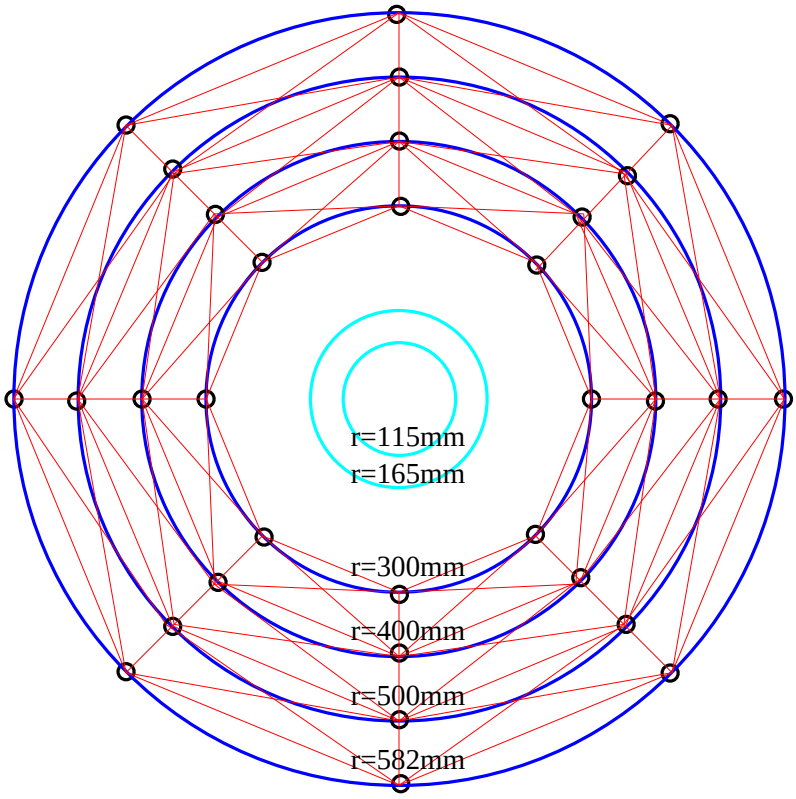

Figure 7: *A possible alignment grid for the end-planes of the Si barrel. It is expected that there will be a thin plane in which the required lines of sight are available. There are 64 variables to be determined (r and ϕ for 32 points), and 104 measurements (13 per octant).*

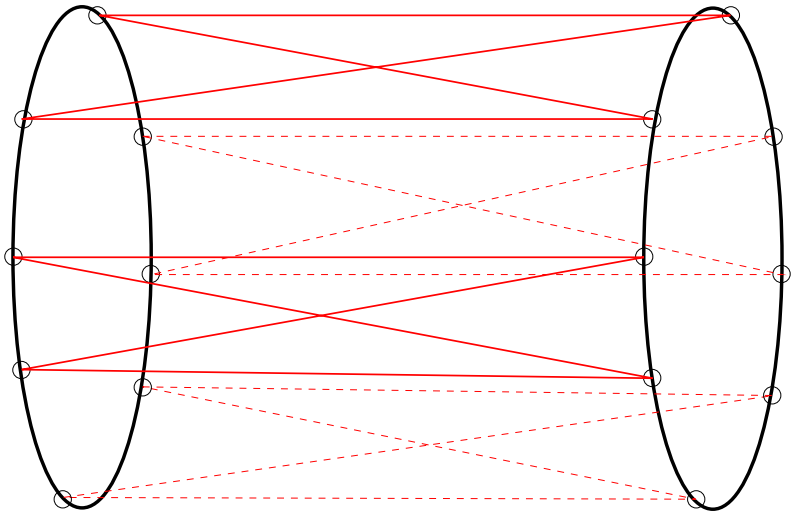

Figure 8: *A possible longitudinal alignment grid. These measurements would ideally be made for each of the 4 cylinders giving 64 measurements in total. An additional plane of measurements may be inserted between the end-planes.*

4 The Laboratory Demonstration System

4.1 Introduction

A laboratory-based demonstration system has been built and tested at Oxford in order to demonstrate the validity of the principles discussed above, and to investigate the issues important in the development of an FSI system for ATLAS.

The system is based around a single fully-remote interferometer illuminated with a tunable semiconductor diode laser operating in the near-infrared part of the spectrum. A photomultiplier is employed to detect the interference fringes. Three étalons and a wavemeter are used to measure the laser frequency. The scan control and data acquisition are based on a Pentium PC with a CAMAC interface. A realistic optical power level and data acquisition bandwidth are used. See Figure 9 and Plate 1.

4.2 Remote interferometer

The design of an interferometer suitable for measuring distances in an inaccessible location in a high-radiation environment has been discussed above in Section 3.2. The interferometer used in the demonstration system is intended to be optically similar to the one proposed for use within ATLAS and therefore employs all of the important elements of the device envisaged for the final system (namely a pair of long single-mode optical fibres, a plate glass beamsplitter and a retroreflector) used within similar operational parameters (namely those of range, power level, and data acquisition bandwidth).

Two fibre ends, one from each of two standard 100 m-long single-mode optical fibres, are mounted parallel about 1 mm apart in a metal block which is secured to a vibration-damped optical table. The two free fibre ends are connected to the laser and to the PMT. The half angle of the gaussian laser cone emitted from the delivery fibre (and conversely the acceptance angle of the return fibre) is about 5 °.

The beamsplitter is a 2 mm-thick glass plate mounted 1–5 cm from the fibre mounting block, and is rotatable about the axis perpendicular to the table.

The retroreflector is a 7.16 mm prism-type corner-cube mounted at a variable range of between 10 cm and 1.5 m from the fibres. See Plate 2.

4.3 Semiconductor diode laser

The choice of laser was forced by the technology which was available at low cost and within a short period of time. The expense and complexity of a Ti:sapphire laser and its associated pump laser would have been unjustified at this early stage, and since high power was not a priority for the demonstration of a single interferometer, a semiconductor laser diode was chosen.

There are two types of semiconductor diode lasers: those based on an optical cavity formed by the cleaved ends of the semiconductor die which contains the laser gain structure, and those in which the optical cavity contains components which are external to the semiconductor. External-cavity diode lasers have the advantage that the tuning is independent of the properties of the semiconductor crystal, and is achieved by precise movement of the external cavity components using piezo-electric actuators under microprocessor control. This technology is at a relatively early stage of development, so the laser which was chosen for the demonstration system is of the non-external-cavity variety. Tuning in this case is rather more crude and is effected by simply varying the temperature

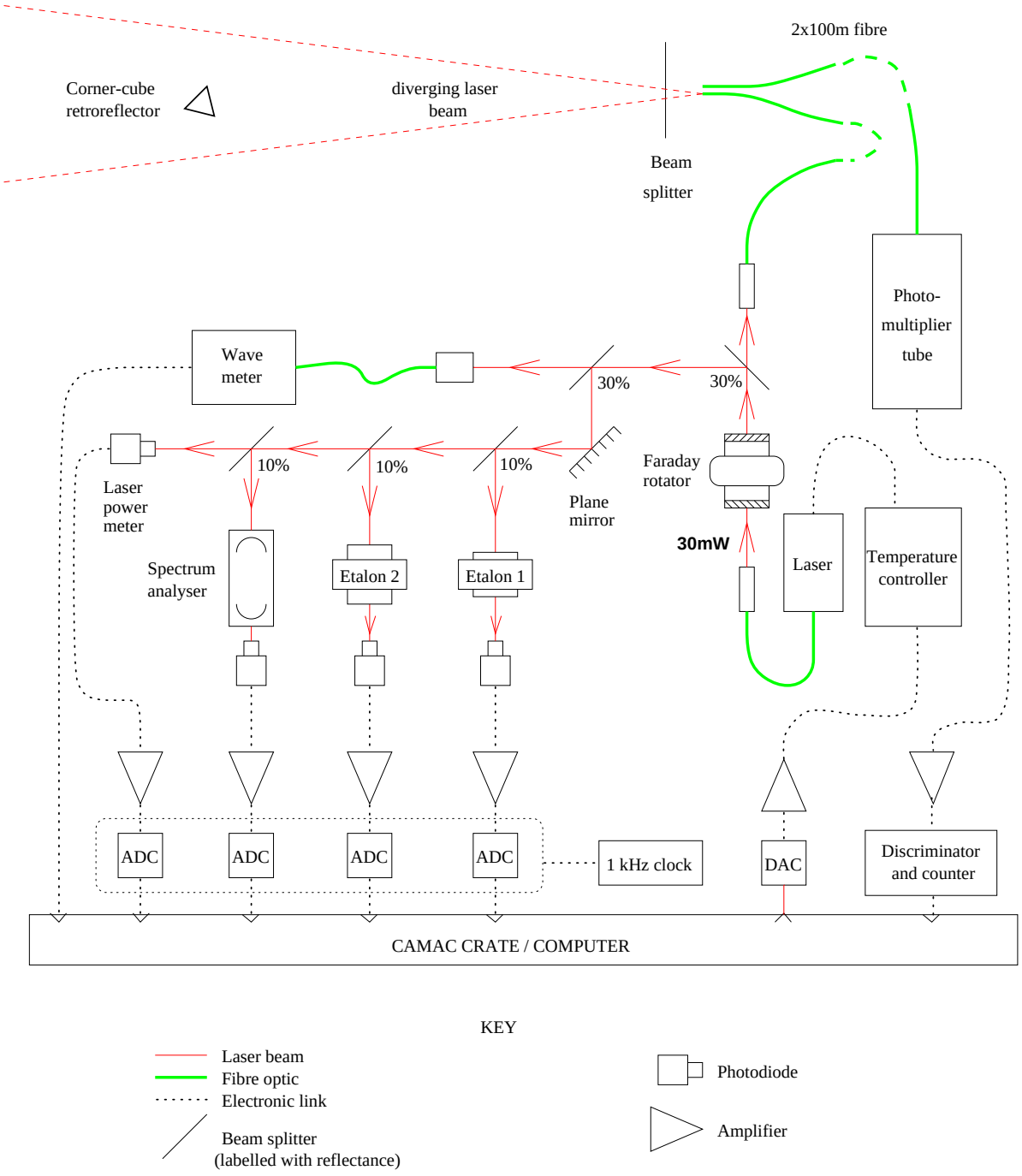

Figure 9: *The FSI laboratory demonstration system.*

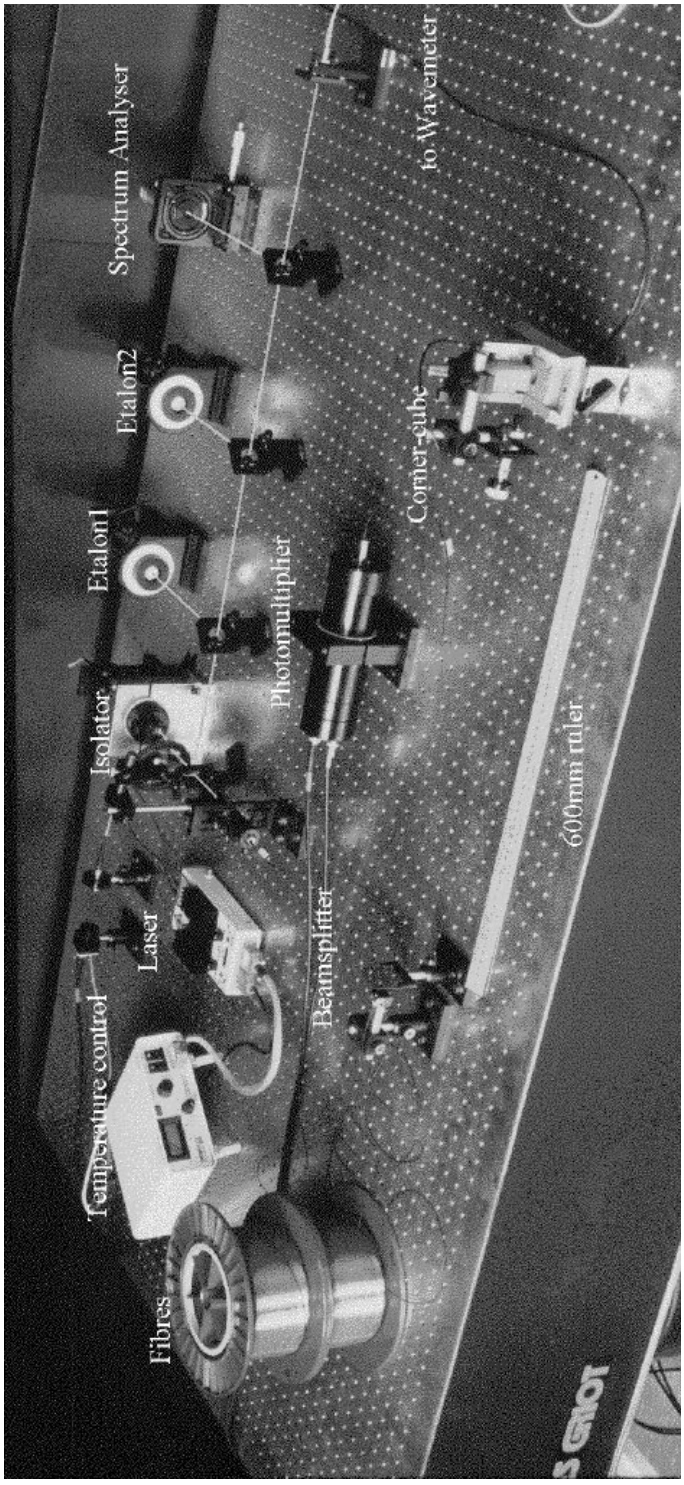

Plate 1: *The FSI demonstration system. In the foreground is the interferometer, set up to measure a 600 mm length. The two drums to the left hand side each hold 100 m of single-mode optical fibre. The smaller white box contains the laser. The larger box to the left of it holds the temperature control electronics. In the background, from left to right, are the étalons, E_1 and E_2, and the spectrum analyser, SA (E_3). The wavemeter is above the table connected by the fibre just visible on the right. The black cylinder in the centre of the table is a light-tight housing containing the photomultiplier tube.*

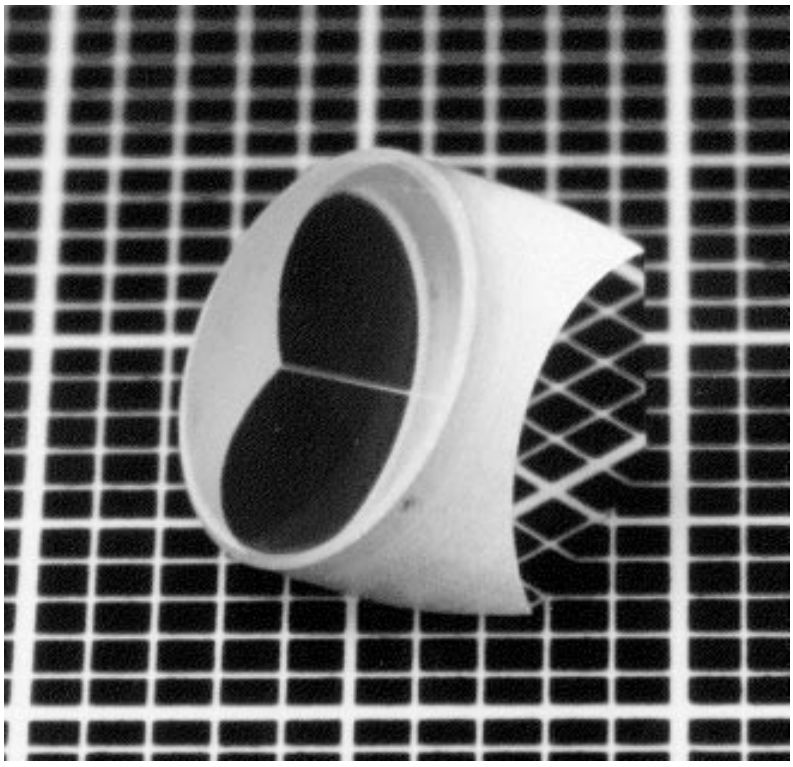

Plate 2: *The corner-cube used in the demonstration system. The diameter of the front face is 7.16 mm.*

of the diode and hence, by thermal expansion, the length of the optical cavity. The device selected for use in the demonstration system has a tuning range of 823–832 nm (5–45 °C), although the mode-hop-free tuning range is much less than this (of order GHz). It delivers an optical power of 30 mW into a fibre — enough to serve the frequency measurement equipment and one interferometer.

A well known problem with semiconductor diode lasers is their hypersensitivity to back-reflected light. In systems where the optics (for example fibre couplers and confocal cavities) need to be aligned perpendicular to the laser beam there is often a considerable amount of light reflected back into the laser. This was found to be the case in the FSI demonstration system, so a Faraday isolator was placed in the beam. This device rejects light reflected back from the frequency measurement equipment using a Faraday polarisation rotation cell and a pair of polarisers.

It was found that when the temperature was ramped the laser did not tune continuously but in a series of small jumps which resulted in small steps appearing in the fringes and in the étalon traces. These frequency skips are probably due to interaction of the laser with light reflected back from the glass-air interface at the end of the short fibre attached directly to the laser.

4.4 Optical frequency measurement

The optical frequency measurement system is essentially the same as that explained in Section 3.6. Three étalons are used to provide high-precision measurements of relative optical frequency. A wavemeter is employed to link these measurements in terms of absolute frequency. The equipment specifications are shown in Table 2.

In order for the system to work, the frequency uncertainty from each device must be

Item	Air gap length	FSR	Finesse	Width of peaks
Wavemeter	—	—	—	eff. 30GHz
Etalon 1	0.6mm	250GHz	100	2.5GHz
Etalon 2	15mm	10GHz	100	100MHz
Spectrum Analyser (E_3)	eff. 75mm	2GHz	100	20MHz

Table 2: *Frequency measurement equipment used in the demonstration system, in order of increasing precision.*

less than half the peak spacing ('free spectral range', FSR) of the next. The wavemeter (accurate to 1 part in 10^4, i.e. ± 30 GHz uncertainty) gives an absolute measure of frequency which is sufficiently accurate for the relative order of E_1 peaks (250 GHz apart) in different sub-scans to be determined exactly. Fitting of the E_1 peaks (likely to be better than the peak width of 2.5 GHz) then allows determination of the relative orders of the E_2 peaks (10 GHz apart). Similarly, fitting the E_2 peaks yields the orders of the E_3 peaks (2 GHz apart). The final frequency measurement precision is then the fitting accuracy of the last étalon – potentially better than 20 MHz in this case.

4.5 Photodetection

As explained in Appendix C, if the optical power supplied to the interferometer is of the order of 10 mW, then the peak power of the detected fringe signal is of the order of 3 pW. Detection of a signal at this level requires a sensitive detector and so a photomultiplier tube (PMT) was chosen. This is used in photon counting mode, with a pulse height discriminator and a CAMAC counter module.

The selected device (a Hamamatsu R943-02) has a GaAs(Cs) photocathode rather than one of the more usual multialkali materials, and as a result is sensitive into the infra-red part of the spectrum and not just the visible region. At 850 nm the radiant sensitivity is 65 mA W^{-1} so for an incident optical power of 3 pW (about 10^7 photons sec^{-1}), the cathode current I_k would be around 200 fA (1.2×10^6 electrons sec^{-1}), corresponding to a quantum efficiency of about 10%.

When a photomultiplier is used in photon counting mode (rather than measuring the cathode current) the signal-to-noise ratio is given by

$$S/N = \frac{N_{sig}\sqrt{T}}{\sqrt{N_{sig} + 2(N_{bkg} + N_{dark})}}$$

where T is the measurement time, and N_{sig}, N_{dark} and N_{bkg} are the count rates for the signal, the dark current and the background respectively.

For the chosen PMT, the dark count rate N_{dark} is around 3×10^4 counts sec^{-1} at 20 °C. For $T = 0.01$ s and $N_{sig} = 10^6$ counts sec^{-1} the expected signal-to-noise ratio is of the order of 100. Since the signal rate is much larger than the dark count, there would be little advantage in operating the PMT at a lower temperature.

4.6 Data acquisition and scan control

The PMT signal is amplified and passed to a pulse height discriminator, the output of which is counted with a CAMAC counter module. PIN photodiodes are used to detect the intensities of the transmitted beams of the three étalons. In addition a beam is extracted

and fed to a fourth photodiode to provide a signal proportional to the laser power. All four signals are amplified and logged via a CAMAC ADC module. The wavemeter output is transmitted directly to the PC via a serial data link.

The FSI scan is effected by ramping the set-point temperature of the laser temperature controller under computer control whilst simultaneously recording data from the PMT, the étalons, the wavemeter and the laser level meter. The laser set-temperature is driven by a DAC card in the PC. See Figure 9.

The scan control and data acquisition are both synchronised to an external quartz oscillator which is used to gate the ADC module. The PC waits for the CAMAC look-at-me (LAM) signal corresponding to the end of the ADC conversion, at which point the DAC is incremented and the ADCs and the PMT pulse counter are read out and reset ready for the next cycle.

4.7 Results

Interferometer

In order to demonstrate that the received signal was indeed sinusoidally dependent on the length R_c between the fibres and the retroreflector, a piezoelectric transducer driven by a triangular voltage ramp was employed to move the corner-cube repeatedly towards and away from the fibres over a distance of a few microns, whilst the laser was held at a fixed wavelength. The received signal was displayed on an oscilloscope. As expected the detected signal varied sinusoidally with the corner-cube position.

Using this setup it was a straightforward matter to investigate how the received signal depended on the positions of the corner-cube and the beamsplitter with respect to the fibre mounting block.

As foreseen the corner-cube could be moved around freely within the gaussian laser cone resulting in a fringe signal with an amplitude dependent upon the fibre-to-retroreflector distance and upon the transverse position of the retroreflector in the laser cone. No precise angular positioning of the corner-cube was needed in order to obtain fringes: due to its large angle of acceptance ($\pm 35°$) it could simply be placed in the beam pointing roughly in the right direction.

The visibility of the fringes could be optimised by rotating the beamsplitter, although fringes could be obtained with a relatively large range of beamsplitter positions and angles.

With an estimated input optical power of 10 mW, a clear fringe signal was detectable up to a range R_c in excess of 1 m. An acceptable signal-to-noise ratio could be maintained at sampling rates of more than 1 kHz (depending on the measured length). See Figures 10 and 11.

Independence of the interference signal from mechanical deformation of the fibres was demonstrated experimentally. (The polarisation of a beam transmitted through a fibre was shown to be very sensitive to the shape of the fibre. However, as explained in Section 3.2, the use of single-mode fibres makes the fringe signal intrinsically insensitive to the fibre shape.)

The received signal was found to be relatively insensitive to the light reflected from objects placed in the laser cone (but not obscuring the line of sight to the retroreflector). It was found that even white objects could be placed in the beam with an acceptably small effect on the received fringe signal.

Operation of the interferometer through a tube was demonstrated successfully : when

a piece of 25 mm diameter black plastic pipe was placed between the fibre head and the retroreflector, an acceptable fringe visibility was maintained — indicating that FSI measurements could be made through tubes if required. Light thin tubes or screens could be used to protect lines of sight or to prevent light leakage between one interferometer and another if this proves to be excessive.

System test

Once the behaviour of the interferometer had been examined and found to be satisfactory, the full system was tested. This involved scanning the laser under computer control whilst recording data in the manner explained in Section 4.6.

Figures 10 and 11 show the fringe intensity I (PMT), the transmitted signals for étalons E_1, E_2 and E_3, and the laser power, all logged at 100 Hz over a period of 320 s. The total change in laser temperature during this period was 3.906 °C corresponding to a change in optical frequency of just over 110 GHz.

The laser has a large number of mode-hops over its tunable range. These are visible as discontinuities in the data and appear simultaneously in all the signals, most visibly in the laser power trace. The short frequency interval between mode-hops and their high number made it impractical to attempt to link the mode-hop-free sections together with the wavemeter as had previously been envisaged. In addition there is the small frequency-skipping effect explained in Section 4.3 which is visible as small steps in the traces (see Figure 11).

Due to the aforementioned limitations of the laser, measurements extracted from data such as that shown in Figures 10 and 11 do not have the full precision. However, there is good reason to expect that the desired resolution will be achieved with a higher performance laser. Such lasers, suitable for use in the final FSI system, have already been described in Section 3.5.

5 Conclusion and Future Work

The survey system presented here is designed to be capable of making high-precision measurements of absolute position of a large number of points within the ATLAS Inner Detector during operation. The underlying measurement technique (FSI) has been described in detail and initial findings from a laboratory-based demonstration system have been presented.

The remote passive interferometer and the fibre-based laser delivery and detection technique have been tested successfully. Thus correct operation of all the intra-detector elements has been demonstrated. Further work is required to finalise the design of the interferometer, the 3D grid and the jewels.

The limitations of the semiconductor laser used in the demonstration system have meant that the required measurement precision has not yet been attained. However, the results are otherwise encouraging. Although the FSI technique cannot yet be claimed as proven at the required precision, the results presented here allow a degree of confidence that the final desired accuracy will be attained when the laser is upgraded. Suitable lasers are known to exist and will be investigated.

The geodetic grid and the general alignment philosophy will be described more fully in further ATLAS Notes. Development of the survey system will continue at Oxford.

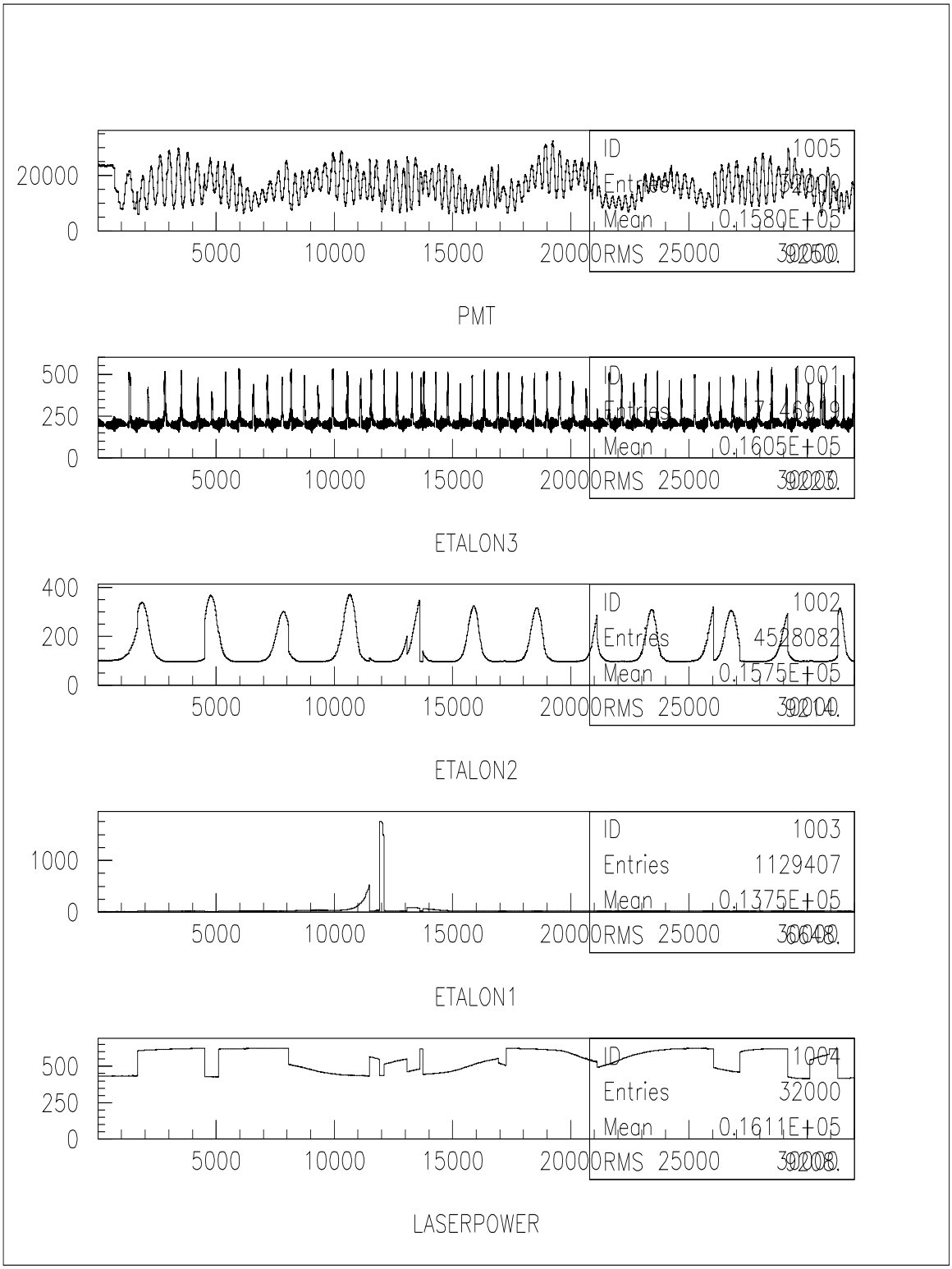

Figure 10: *Data taken with the demonstration system. The temperature was scanned from* $20.500\,^{o}C$ *to* $24.406\,^{o}C$ *over a period of 320 seconds. Data was logged at 100Hz. The étalons have been misaligned to reduce the sharpness of the peaks for clarity. The discontinuities in the laser power level correspond to mode-hops — i.e. discontinuities in optical frequency.*

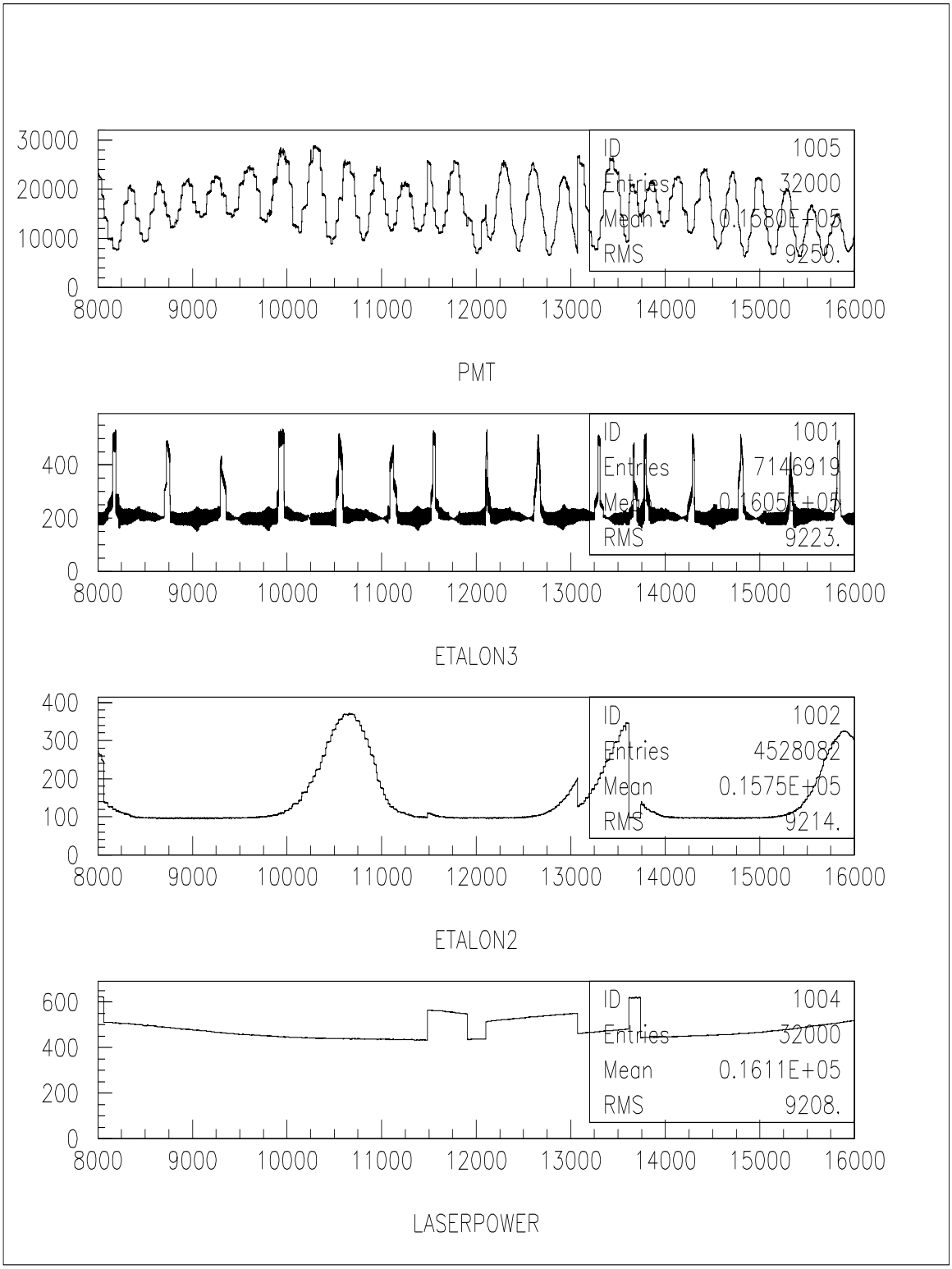

Figure 11: *A section of the data shown in Figure 10. The small steps visible in the plots (particularly the PMT and ETALON2 traces) are due to a frequency stepping effect of the laser (see Section 4.3). The digitisation and the temperature ramp steps take place on a much shorter time scale.*

Appendix A : Optical path calculations

It is imperative that the geometry of the interferometer be examined in order to investigate the factors influencing the value of the measured length. In doing so, one may note an important consequence of the use of single mode fibres : since the core diameter of the fibres is small compared to the wavefront curvature and the angle of incidence of the rays on the fibre ends is small, the phase variation across the surface of the receiving fibre is also small, and so the phase of the signal transmitted down the fibre can be approximated by the phase of the single ray which hits the centre of the fibre end. The same principle applies for both sending and receiving fibres. Hence to calculate the phase of the interference signal it is only necessary to evaluate the optical path lengths for one ray in each of the interfering beams.

In the following sections, the total optical path lengths of light rays in the measurement beam and in the reference beam are calculated. It is assumed here that the corner-cube is of the externally reflecting variety and that the three reflecting faces are accurately plane and at exactly 90° to each other.

Measurement beam

Figure 12 explains the reflection of a point object in a corner-cube. If α is the angle the incident beam makes with the first reflective surface that it hits, then it can be seen that

$$\begin{aligned} |\overrightarrow{IF}| &= |\overrightarrow{IC}| \cos\alpha = |\overrightarrow{IE}| \cos^2\alpha \\ |\overrightarrow{EG}| &= |\overrightarrow{EC}| \sin\alpha = |\overrightarrow{IE}| \sin^2\alpha \\ \Rightarrow |\overrightarrow{IE}| &= |\overrightarrow{IF}| + |\overrightarrow{EG}| \end{aligned} \tag{18}$$

So the emerging ray has the same path length as it would have had it continued to F and emerged anti-parallel from the point G. That is, the corner-cube can be said to be equivalent to a reflection from the plane perpendicular to the incident ray which passes through the corner-point C, combined with an inversion of the reflection point through C, i.e. F is translated to G.

Now if A' is the reflection of A in C, it is clear that

$$\overrightarrow{AF} = -\overrightarrow{A'G} \tag{19}$$

Therefore the emerging ray has a direction and phase consistent with it having been emitted from the image point A', and so the calculation of the total path length of a ray emitted at A and received at B after multiple reflections in a corner-cube requires only the calculation of the single length $A'B$.

$$|\overrightarrow{AI}| + |\overrightarrow{IE}| + |\overrightarrow{EB}| = |\overrightarrow{A'B}| \tag{20}$$

Figure 13 illustrates the use of the corner-cube in the FSI interferometer.

$$\overrightarrow{OA} = (0, y_{fib}, 0)$$

$$
\begin{aligned}
\overrightarrow{OB} &= (0, -y_{fib}, 0) = -\overrightarrow{OA} \\
\overrightarrow{OC} &= (R_c, \theta_c, \phi_c) \text{ in spherical polar coordinates} \\
&= (R_c \sin\theta_c \cos\phi_c, R_c \sin\theta_c \sin\phi_c, R_c \cos\theta_c) \text{ in cartesian coordinates} \\
\overrightarrow{AC} &= \overrightarrow{OC} - \overrightarrow{OA} \\
\overrightarrow{OA'} &= \overrightarrow{OA} + 2\,\overrightarrow{AC} \\
\overrightarrow{A'B} &= \overrightarrow{OB} - \overrightarrow{OA'} \\
&= \overrightarrow{OB} - (\overrightarrow{OA} + 2\,\overrightarrow{AC}) \\
&= \overrightarrow{OB} - \overrightarrow{OA} - 2(\overrightarrow{OC} - \overrightarrow{OA}) \\
&= \overrightarrow{OB} - \overrightarrow{OA} - 2\,\overrightarrow{OC} + 2\,\overrightarrow{OA} \\
&= -2\,\overrightarrow{OC} \\
\Rightarrow |\overrightarrow{A'B}| &= 2R_c
\end{aligned} \tag{21}
$$

That is, if the effect of the beamsplitter is ignored, the total optical path length of a ray which leaves the delivery fibre, which is reflected by the corner-cube, and which enters the receiving fibre is equal to twice the distance between the corner point and the point midway between the two fibres, independent of the angular position of the corner-cube with respect to the fibres, and independent of the separation of the fibres.

Figure 14 illustrates the refractive effect of the beamsplitter. The total optical path length ($\mathcal{OPL}$) now involves angular terms related to the distance the light travels inside the beamsplitter :

$$
\begin{aligned}
x_c &= x_b + d + x_{SC} \\
n_2 \sin\theta_2 &= n_1 \sin\theta_1 \\
\mathcal{D}_1 = \mathcal{OPL}\,(A \longrightarrow (C) \longrightarrow B) &= 2(n_1\,|\overrightarrow{AT}| + n_2\,|\overrightarrow{TP}| + n_1\,|\overrightarrow{SC}|) \\
&= 2\left(\frac{n_1 x_b}{\cos\theta_1} + \frac{n_2 d}{\cos\theta_2} + \frac{n_1 x_{RC}}{\cos\theta_1}\right) \\
&= 2\left(\frac{n_2 d}{\cos\theta_2} + \frac{n_1 (x_c - d)}{\cos\theta_1}\right) \\
&= 2\left(n_1 R_c + d\left[\frac{n_2}{\cos\theta_2} - \frac{n_1}{\cos\theta_1}\right]\right)
\end{aligned} \tag{22}
$$

Reference beam

See Figure 15. As is the section above there are two similar triangles in the ratio 2 : 1, AOM and ABA'', with common angle OAM. Clearly $A''B = 2OM$.

$$
\begin{aligned}
\mathcal{D}_2 = \mathcal{OPL}\,(A \longrightarrow R \longrightarrow B) &= n_1\,|\overrightarrow{A''B}| \\
&= 2n_1\,|\overrightarrow{OM}| \\
&= 2n_1\,|\overrightarrow{OA}|\cos(\delta - \alpha) + 2n_1\,|\overrightarrow{AM}|\cos\alpha
\end{aligned}
$$

$$
\begin{aligned}
&= 2n_1 r_b(\sin\alpha\cos(\delta-\alpha)+\sin(\delta-\alpha)\cos\alpha) \\
&= 2n_1 r_b\cos\theta \qquad (23)
\end{aligned}
$$

Where θ is the angle of deviation of the beamsplitter away from being normal to the fibre axis, $\delta = \frac{\pi}{2} - \theta$, and $r_b^2 = |\overrightarrow{AN}|^2 = x_b^2 + y_{fib}^2$, i.e. the distance from the point A to the point where the beamsplitter intersects the fibre axis. The total optical path length of the reference beam is effectively what is measured in the laboratory calibration. It is a constant for any given fibre/beamsplitter unit.

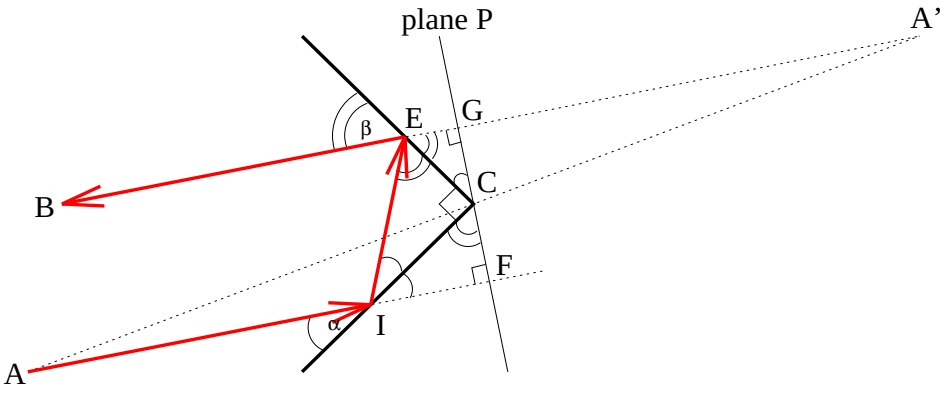

Figure 12: *Geometry of the reflection of a single ray from a corner-cube. The reflected ray is parallel to the incident ray but reversed in direction. The plane P is perpendicular to the incident and reflected rays and passes through the vertex of the corner-cube C. The path length is the same as it would be had the ray continued to F and emerged anti-parallel from G, i.e. the corner-cube is equivalent to a reflection from the plane P combined with an inversion through C. Alternatively the image A' of A may be used. It is found by reflecting A in C.*

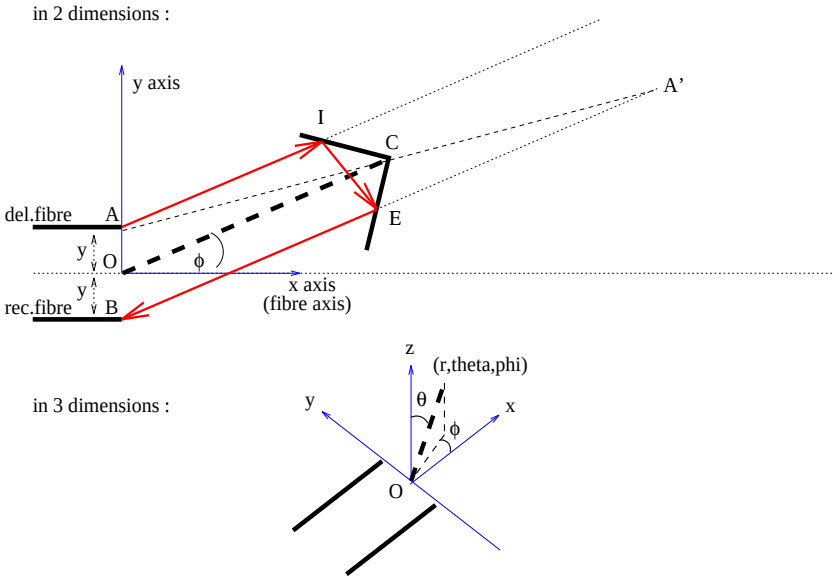

Figure 13: *Geometry of the reflection of a ray emitted from the delivery fibre at A and hitting the return fibre at B, in the simplified case where the effect of the beamsplitter is considered negligible. The total path length $\mid A \rightarrow I \rightarrow E \rightarrow B \mid = 2 \mid \overrightarrow{OC} \mid = 2R_c$ independent of the angular position of C in space and independent of the fibre separation, $2y_{fib}$.*

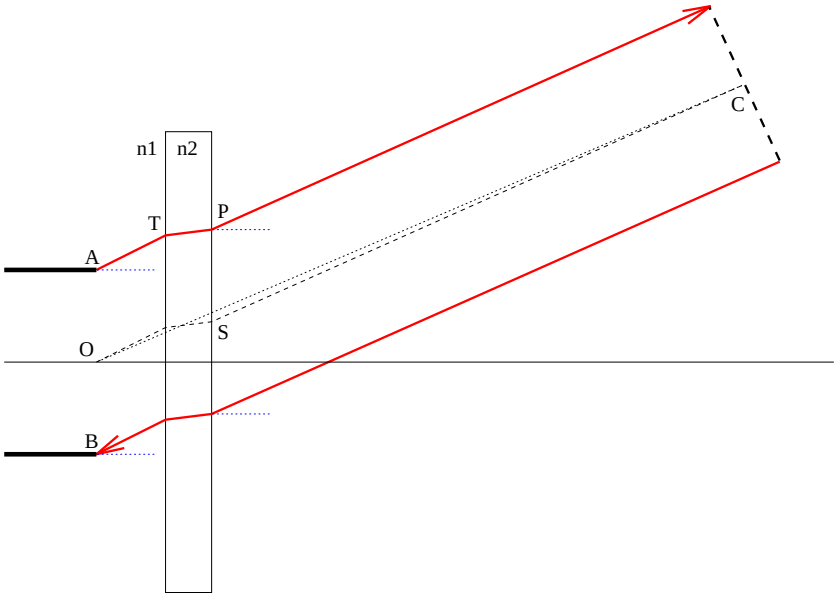

Figure 14: *Geometry of the corner-cube ray including refraction due to the beamsplitter. The total optical path length* $\mathcal{OPL}(A \longrightarrow B) = 2\left(n_1 R_c + d\left(\frac{n_2}{\cos\theta_2} - \frac{n_1}{\cos\theta_1}\right)\right)$ *where* $R_c = |\overrightarrow{OC}|$ *and* $n_1 \sin\theta_1 = n_2 \sin\theta_2$.

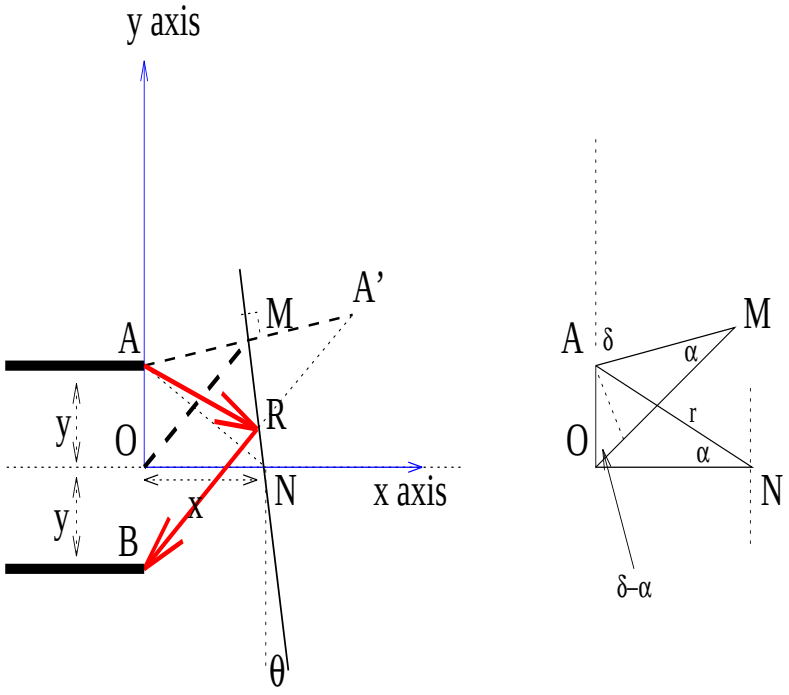

Figure 15: *Geometry of the beamsplitter ray. The total optical path length* $\mathcal{OPL}(A \rightarrow R \rightarrow B) = 2n_1\ |\overrightarrow{OM}| = 2n_1 r_b \cos\theta_b$ *where* $r_b^2 = |\overrightarrow{AN}|^2 = x_b^2 + y_{fib}^2$ *and* θ_b *is the angle by which the beamsplitter deviates from parallel to the y axis. This is a constant for any given fibre/beamsplitter unit and will be measured during the laboratory calibration.*

Appendix B : The Phase-Shift Technique

In order to attain the required measurement precision, it will be necessary to measure the total phase change during the FSI scan to an accuracy of $\frac{2\pi}{100}$. The critical dependence of the measurement precision upon this phase accuracy and the possibility that the interferometer signal could be rendered useless by the presence of vibrations with an amplitude of the order of one half-wavelength (i.e. less than the length measurement resolution) have led to the consideration of a direct phase measurement technique. This is designed to provide immunity to vibrations whilst maintaining the phase accuracy.

In the absence of significant vibration it would be possible to simply scan the laser wavelength monotonically and to log and fit the received fringe intensity in order to extract the phase of any given point. However the possible presence of vibrations larger than $\frac{\lambda}{2}$ has led to consideration of a modified version of a technique known variously as 'direct phase detection', 'phase-shift interferometry (PSI)', 'digital wavefront measurement' or 'phase-stepping' [63]–[79]. Conventionally the technique involves directly changing the fringe phase ϕ of the received signal I by altering the optical path length of either the reference beam or the measurement beam by a known amount. Since the received fringe intensity varies cosinusoidally with the optical path difference, it is possible to calculate ϕ if I is measured for several known values of $\delta\phi$.

The change in path length is commonly achieved by using a piezo-electric actuator to move a mirror by a fraction of a wavelength. In the present system however, there is no access to either the reference beam or the measurement beam, both being remote and having rigid path lengths. Nevertheless, the phase-shift technique may still be applied by using a small change in the laser frequency to produce the required phase change. It is expected that an acousto-optic modulator will be used to shift the laser wavelength by a variable amount under electronic control [68].

The received intensity is given by

$$I(t) = P\left\{f_b^2 + f_c^2 + 2f_b f_c \cos\left[\frac{2\pi(\mathcal{D}_{12} + 2x_{vib}(t))}{\lambda}\right]\right\} \tag{24}$$

where P is proportional to the power delivered into the interferometer, f_b and f_c are the fractions of the incident power returned from the beamsplitter and the corner-cube respectively, $\mathcal{D}_{12}$ is the optical path difference in the absence of vibration and $x_{vib}(t)$ represents any vibration of the interferometer dimensions or turbulence in the gaseous medium. This is more conveniently written as

$$I = I_0\{1 + \gamma_0 \cos\Phi(t)\} \tag{25}$$

where I_0 is the d.c. intensity, γ_0 is the magnitude of the fringe modulation, and the fringe phase $\Phi(t)$ is given by

$$\Phi(t) = \frac{2\pi(\mathcal{D}_{12} + 2x_{vib}(t))}{\lambda} \tag{26}$$

Whatever the form of the vibration/turbulence/noise represented by x_{vib}, there exists a mean interferometer phase $\langle\Phi(t)\rangle$, corresponding to a mean optical path difference, and to a mean measured length. The cosine in Equation 25 complicates the extraction of the mean phase $\langle\Phi(t)\rangle$, since any technique applied to extract a phase from an interferometer fringe pattern returns not Φ but ϕ where

$$\phi = \Phi \bmod 2\pi \tag{27}$$

Simple averaging of the received intensity I or of the phase ϕ is useless since taking the average of the modulus of a distribution will not return the correct value for the average value of the distribution, that is

$$\langle \phi(t) \rangle \neq \langle \Phi(t) \rangle \tag{28}$$

In order to extract Φ and hence $\langle \Phi \rangle$, the 2π modulus must be resolved by tracking ϕ across the boundaries where it changes abruptly from 2π to 0 and *vice versa* and correcting subsequent measurements by adding or subtracting 2π. This process is known as 'phase unwrapping' and Φ is known as the 'unwrapped phase'. Clearly the rate of measurement of ϕ must be sufficiently high for ϕ not to have changed by more than π between measurements. Hence if phase-shifting interferometry is to be used, the phase-shifting must operate faster than the vibration or, put another way, for a given rate of phase-shifting there is a maximum possible vibration frequency which can be analysed.

The following analysis shows the general technique for extracting the phase ϕ from a set of phase-shifted measurements of fringe intensity I.

If $\delta\nu_i$ is the ith frequency shift in a series of N shifts, then the interferometer phase ϕ and phase-shift $\delta\phi_i$ are given by

$$\begin{aligned} \phi &= \frac{2\pi\nu}{c}(\mathcal{D}_{12} + 2x_{vib}) \\ \phi_i &= \phi - \delta\phi_i = \frac{2\pi(\nu - \delta\nu_i)}{c}(\mathcal{D}_{12} + 2x_{vib}) \\ \delta\phi_i &= \frac{2\pi\delta\nu_i}{c}(\mathcal{D}_{12} + 2x_{vib}) \approx \frac{2\pi\delta\nu_i}{c}\mathcal{D}_{12} \end{aligned} \tag{29}$$

So for a measurement range R_c of 1 m a phase shift $\delta\phi$ of π requires a frequency shift $\delta\nu$ of 75 MHz.

Unless truly discrete phase steps are used, the detector will integrate the fringe intensity over a phase shift range Δ. The recorded intensity is then

$$\begin{aligned} I_i &= \frac{1}{\Delta}\int_{\delta\phi_i - \frac{\Delta}{2}}^{\delta\phi_i + \frac{\Delta}{2}} I_0\{1 + \gamma_0 \cos[\phi + \delta\phi(t)]\}\, \mathrm{d}(\delta\phi(t)) \\ &= I_0\{1 + \gamma_0 \operatorname{sinc}\frac{\Delta}{2}\cos[\phi + \delta\phi_i]\} \end{aligned} \tag{30}$$

If discrete steps are used then $\Delta = 0$ and the sinc function has a value of unity. Consider an alternative representation of this received fringe intensity [64][77]

$$I_i = a_0 + a_1 \cos\delta\phi_i + b_1 \sin\delta\phi_i \qquad i = 1, 2, \ldots, N \tag{31}$$

where

$$\begin{aligned} a_0 &= I_0 \\ a_1 &= I_0\gamma_0 \operatorname{sinc}\frac{\Delta}{2}\cos\phi \\ a_2 &= I_0\gamma_0 \operatorname{sinc}\frac{\Delta}{2}\sin\phi \end{aligned} \tag{32}$$

The least-squares solution to this set of simultaneous equations is then

$$\begin{pmatrix} a_0 \\ a_1 \\ a_2 \end{pmatrix} = \mathrm{A}^{-1}\mathrm{B} \tag{33}$$

where

$$\mathrm{A} = \begin{pmatrix} N & \sum_i \cos\delta\phi_i & \sum_i \sin\delta\phi_i \\ \sum_i \cos\delta\phi_i & \sum_i \cos^2\delta\phi_i & \sum_i \cos\delta\phi_i \sin\delta\phi_i \\ \sum_i \sin\delta\phi_i & \sum_i \cos\delta\phi_i \sin\delta\phi_i & \sum_i \sin^2\delta\phi_i \end{pmatrix} \tag{34}$$

and

$$\mathrm{B} = \begin{pmatrix} \sum_i I_i \\ \sum_i I_i \cos\delta\phi_i \\ \sum_i I_i \sin\delta\phi_i \end{pmatrix} \tag{35}$$

Hence the phase may be calculated to within modulus 2π :

$$\tan\phi = \frac{a_2}{a_1} = \frac{I_0\gamma_0 \operatorname{sinc}\frac{\Delta}{2}\sin\phi}{I_0\gamma_0 \operatorname{sinc}\frac{\Delta}{2}\cos\phi} \tag{36}$$

$$\Phi = \arctan_2(a_2, a_1) + 2n\pi \tag{37}$$

where n is any integer and $\arctan_2$ is the equivalent of the FORTRAN ATAN2 function which returns ϕ to within modulus 2π (not just π) by checking the signs of the numerator and denominator. Phase unwrapping then returns Φ by keeping track of n.

Since there are three unknowns ($\{I_0, \gamma_0, \phi\}$ or $\{a_0, a_1, a_2\}$) the minimal number of phase steps which can be used is three. The use of a greater number of steps leads to greater accuracy in the phase determination, or equivalently the same accuracy for ϕ for a less precise knowledge of the phase shifts $\delta\phi_i$. It is expected that 5–10 steps will be used, arranged in such a way as to ensure three or more useful steps for each of the measurement lengths, which are likely to vary in value by about a factor three.

Once the phase unwrapping has been used to extract Φ from ϕ, values of Φ from the whole FSI scan may be plotted against the laser frequency and fitted to a straight line. See Figure **??**. The optical path difference is simply given by the gradient of this line :

$$\mathcal{D}_{12} = \mid \mathcal{D}_1 - \mathcal{D}_2 \mid = \frac{c}{2\pi}\frac{\mathrm{d}\Phi}{\mathrm{d}\nu} \tag{38}$$

In this way the effect of vibration is eliminated and the path difference corresponding to the average positions of the optical components is found.

Example

A vibration with a single frequency component may be written as

$$x_{vib}(t) = a_{vib}\cos(2\pi f_{vib}t + \phi_{vib}) \tag{39}$$

where f_{vib}, a_{vib} and ϕ_{vib} are the frequency, amplitude and phase of the vibration respectively. The frequency of the detected interferometer fringes is given by

$$f_{det} = 2\frac{a_{vib} f_{vib}}{\lambda} \tag{40}$$

and the maximum velocity during the motion is

$$\left.\frac{dx_{vib}(t)}{dt}\right|_{max} = 2\pi f_{vib} a_{vib} \tag{41}$$

For a vibration with a single frequency component at 100 Hz and an amplitude $a_{vib} = 1.0\mu$m, the detected fringe frequency would be $\frac{4\times100\times1.000}{0.830/2} = 964$ Hz. At a wavelength of 830 nm a sampling frequency of 10 kHz would be sufficient to detect vibrations with a frequency-amplitude product up to around 100 Hz μm, which corresponds to a maximum velocity of about 0.6 mm s^{-1}.

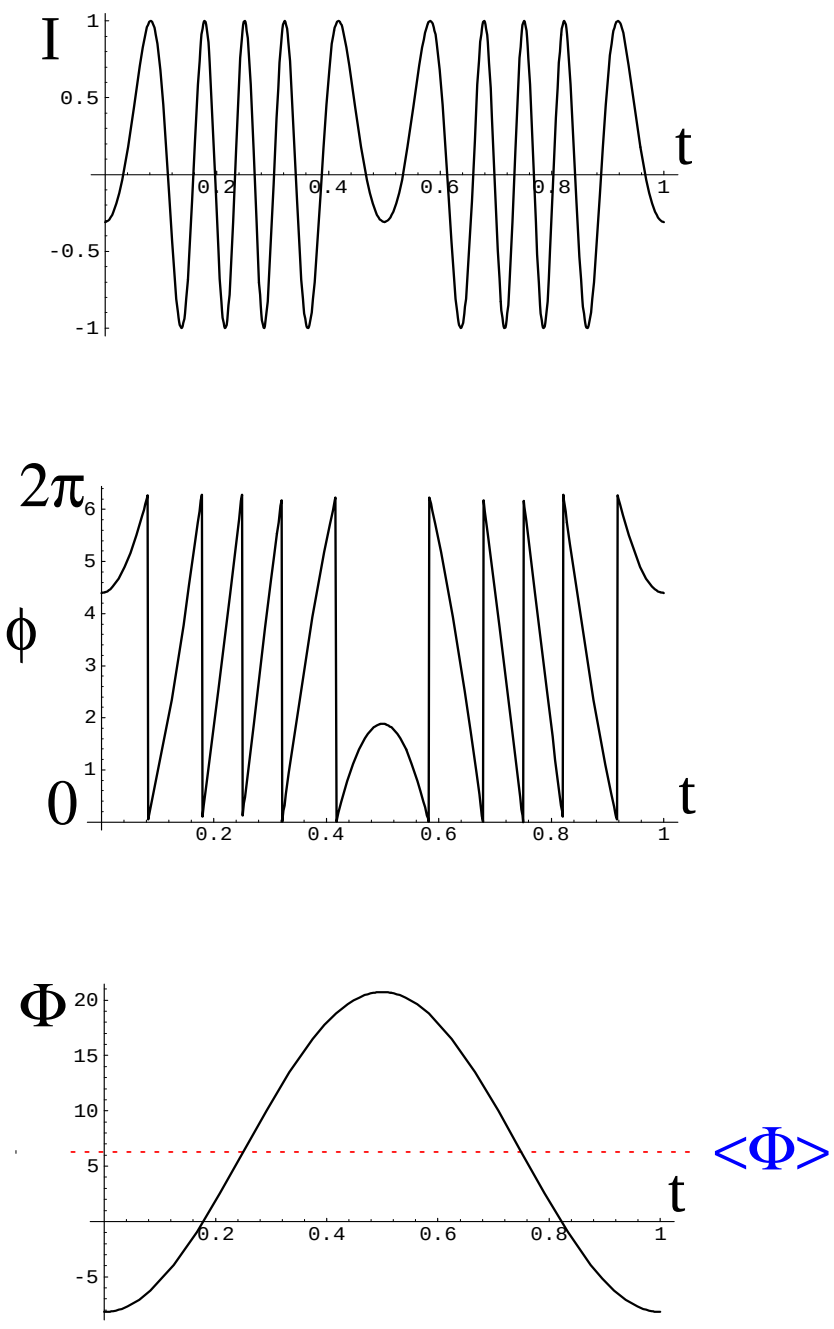

Figure 16: *Example plots of (a) the fringe intensity I versus time (ignoring the d.c. offset I_0), (b) the fringe phase ϕ, and (c) the unwrapped phase Φ, for vibration with a single frequency component. The vibratory motion reverses direction every half-unit on the horizontal (time) axis. The peak-peak amplitude of the vibration is 4.6 half-wavelengths.*

Appendix C : Detecting the interference signal

The measurement precision depends upon the accuracy with which the phase of the interferometer fringes can be determined. This is a matter of laser power, geometrical efficiency, fringe visibility, and detector signal-to-noise ratio.

It is useful to define a 'geometrical efficiency' g for the interferometer as the fraction of the light emitted from the delivery fibre which hits the return fibre, ignoring all non-geometrical losses. The overall optical efficiency is then given by the product of the geometrical efficiency and a factor representing the reflection losses at the boundaries between materials and the losses due to scattering.

The geometrical efficiency may be written as $g = g_1 g_2$ where g_1 is the fraction of the emitted light cone which hits the corner-cube, and g_2 is the fraction of the light returned from the corner-cube which hits the return fibre. The dimensions important in the calculation of g are the core radius a and the numerical aperture $NA \stackrel{\text{def}}{=} \sin\theta_{beam}$ of the fibres, the active diameter d of the corner-cube, and the measurement range R_c. The relationships between the numerical aperture, the core radius and the single mode operation of an optical fibre are given in Appendix D.

If the fibre pair is positioned at $x = 0$ pointing along the positive x-axis, and the retroreflector is situated on the x-axis at $x = R_c$, then the circle made by the laser cone in the plane of the corner-cube has a diameter $2R_c \tan\theta_{beam}$. The fraction of the light emitted by the laser delivery fibre which is returned towards the fibre pair by the corner-cube is given by

$$g_1 = \left(\frac{d}{2R_c \tan\theta_{beam}}\right)^2$$

where the d is the diameter of the corner-cube aperture.

The light intercepted by the corner-cube is returned to the fibre head as if coming from a point source at $x = 2R_c$ through a circular aperture with the same diameter (d) as the corner-cube situated at $x = R_c$, resulting in a spot with diameter $2d$ in the plane $x = 0$. If the return fibre has radius a then

$$g_2 = \left(\frac{a}{d}\right)^2$$

Hence the overall geometrical efficiency is given by

$$g = g_1 g_2 = \frac{a^2}{4R_c^2 \tan^2\theta_{beam}}$$

Note that the corner-cube diameter cancels out : a smaller retroreflector would intercept less of the incident light, but would return it towards the fibres in a proportionately more concentrated beam. Values of g for different measured distances R_c are given in Table 3.

Non-geometrical losses account for about a factor two reduction in the optical power of each of the two beams. See Table 4. Maximal fringe modulation is attained when the position and angle of the beamsplitter are such that the returned signal due to the reference beam alone is equal to that of the measurement beam. In this case the fraction of the input power received at the photodetector at a fringe peak is $4 \times 0.49 \times g = 1.96 \times g$. For a measurement range R_c =1 m the overall signal attenuation factor would be $3.2\ 10^{-10}$. So for an injected laser power of 10 mW, the peak received signal power would be 3.2 pW.

Measurement length R_c	Geometrical efficiency g
50 cm	$6.25\,10^{-10}$
100 cm	$1.56\,10^{-10}$
150 cm	$0.69\,10^{-10}$

Table 3: Geometrical efficiency, g for two bare fibres with numerical aperture, NA=0.1, and core radius $a = 2.5\,\mu$m

Item	Efficiency
attenuation in 100 m fibre @4dB/km	0.91
back reflection at fibre end	0.96
beam splitter forward transmission	0.96
delivery fibre to corner-cube geometrical factor	g_1
corner-cube triple-reflectivity	0.70
beam splitter reverse transmission	0.96
corner-cube to return fibre geometrical factor	g_2
back reflection at fibre end	0.96
attenuation in 100 m fibre @4dB/km	0.91
overall efficiency	$0.49 \times g$

Table 4: Overall optical efficiency at a measurement length $R_c = 1$m for two fibres with numerical aperture NA=0.1, and core diameter $a = 2.5\mu$m.

Appendix D : Single mode fibres

The 'numerical aperture', NA, of an optical fibre is given by

$$\text{NA} \stackrel{\text{def}}{=} \sin\theta_{max} = \sqrt{n_{core}^2 - n_{cladding}^2}$$

where θ_{max} is the half angle of a beam emerging from the fibre (or conversely the maximum acceptance angle for an incoming ray), and n_{core} and $n_{cladding}$ are refractive indices. A typical value of the numerical aperture for a single mode fibre is NA= 0.1. The 'V-value' or 'normalised frequency' of a fibre is given by

$$V = ka(\text{NA})$$

where $k = \frac{2\pi}{\lambda}$ and a is the core radius. It can be shown that the condition for single mode operation is

$$V < V_{crit} = 2.405$$

or alternatively for a given wavelength and numerical aperture

$$a < a_{crit} = \frac{2.405\lambda}{2\pi(\text{NA})}$$

If $\lambda = 830\,$nm and NA=0.1 then $a_{crit} = 3.2\,\mu$m. A typical value for the core radius of a single mode fibre is $a = 2.5\,\mu$m.

References

[1] Monitoring of the Alignment of the Inner Detector, C. Daum, NIKHEF, INDET-TR-076, 12 Nov. 1993.

[2] The performance specifications of the ATLAS Inner Detector, D. Froidevaux, A. Parker, ATLAS Internal Note, INDET-NO-046, 6 May 1994.

[3] Alignment of the ATLAS Inner Detector, C. Daum, NIKHEF, ATLAS Internal Note, INDET-NO-060, 12 Sep. 1994.

[4] The ATLAS Technical Proposal, CERN, December 1994.

[5] Alignment of the ATLAS detector from Inner Detector to muon spectrometer, C. Daum, NIKHEF, ATLAS Internal Note, TECH-NO-013, 7 Nov. 1994.

[6] Least square fit and covariance matrix for an octagonal alignment grid for the ATLAS detector, C. Daum, NIKHEF, ATLAS Internal Note, TECH-NO-014, 23 Feb. 1995.

[7] Alignment of the DELPHI vertex detector, V. Chabaud, CERN.

Multiple Frequency Interferometric Metrology

[8] J.R. Benoit, Journ. de Phys. (**3**)**7** (1898) 57.

[9] Principles of Optics, Max Born and Emil Wolf, page 290, Pergamon Press, 1959.

[10] The refractive index of air, B. Edlén, Metrologia **2** (1966) 71–80.

[11] Two-reference-beam holographic interferometry, R. Dändliker, E. Marom and F.M. Mottier, J.Opt.Soc.Am. **66** (1976) 23.

[12] Absolute distance measurements by CO_2 laser multiwavelength interferometry, G.L. Bourdet and A.G. Orszag, Applied Optics **18** (1979) 225–227.

[13] Absolute distance measurement by variable wavelength interferometry, F. Bien, M. Camac, H.J. Caulfield and S. Ezekiel, Applied Optics **20** (1981) 400–403.

[14] Infrared He-Xe laser interferometry for measuring length, Hirokazu Matsumoto, Applied Optics **20** (1981) 231–234.

[15] Synthetic millimeter-wave signal generation for length measurement, Hirokazu Matsumoto, Applied Optics **23** (1984) 973–974.

[16] Two-wavelength phase shifting interferometry, Yeou-Yen Cheng and James C. Wyatt, Applied Optics **23** (1984) 4539–4543.

[17] Optical ranging by wavelength multiplexed interferometry, C.C. Williams and H.K. Wickramsinghe, J. Appl. Phys. **60** (1986) 1900–1903.

[18] Distance measurement by the wavelength shift of laser light, Hisao Kikuta, Koichi Iwata and Ryo Nagata, Applied Optics **25** (1986) 2976–2980.

[19] Fiber-optic interferometer using frequency-modulated laser diodes, Glenn Beheim, Applied Optics **25** (1986) 3469–3472 .

[20] Absolute distance measurement by wavelength shift interferometry with a laser diode : some systematic error sources, Hisao Kikuta, Koichi Iwata, and Ryo Nagata, Applied Optics **26** (1987) 1654–1660.

[21] Interferometer for measuring displacement and distance, Toshihiro Kubota, Makoto Nara and Toshihiko Yoshino, Optics Letters **12** (1987) 310–312.

[22] Two-wavelength laser interferometry using superheterodyne detection, R. Dändliker, R. Thalmann and D. Prongué, Optics Letters **13** (1988) 339–341.

[23] Heterodyne interferometry with a frequency-modulated laser diode, Jun Chen, Yukihiro Ishii and Kazumi Murata, Applied Optics **27** (1988) 124–128.

[24] Absolute optical ranging with 200 nm resolution, C.C. Williams and H.K. Wickramsinghe, Optics Letters **14** (1989) 542–544.

[25] Interferometric absolute distance measurement utilizing a mode-jump region of a laser diode, K. Seta and B.K. Ward, Opt. Comm. **77** (1990) 275–278.

[26] Optical-heterodyne displacement measurement using a frequency-ramped laser diode, Masaaki Imai and Koji Kawakita, Optics Communications **78** (1990) 113–117.

[27] Interferometric determination of a static optical path difference using a frequency swept laser diode, Ryoji Ohba, Ichiro Uehira and Sei-ich Kakuma, Meas. Sci. Technol. **1** (1990) 500–504.

[28] Synthetic wavelength stabilization for two-colour laser-diode interferometry, Peter de Groot and Stanley Kishner, Applied Optics **30** (1991) 4026–4032.

[29] Recent advances in displacement measuring interferometry, N. Bobroff, Meas. Sci. Technol. **4** (1993) 907–926.

[30] External frequency modulation of a laser source for non-incremental interferometric measurements, Letizia De Maria and Mario Martinelli, Meas. Sci. Technol. **4** (1993) 1228–1231.

[31] Laser interferometry for precision engineering metrology, P. Gill, Chapter 5, Optical Methods in Engineering Metrology, edited by D.C. Williams, Chapman & Hall, London 1993, ISBN 0 412 39640 8.

[32] Length metrology using optically-narrowed swept frequency laser diodes, G.P. Barwood, P. Gill and W.R.C. Rowley, Presented at Laser Dimensional Metrology, Photonex '93, Brighton, UK, 5–7 October 1993.

[33] Laser diodes for length determination using swept-frequency interferometry, G.P. Barwood, P. Gill and W.R.C. Rowley, Meas. Sci. Technol. **4** (1993) 988–994.

[34] Tunable, double-wavelength heterodyne detection interferometer for absolute-distance measurements, E. Gelmini, U. Minoni, and F. Docchio, Optics Letters **19** (1994) 213–215.

[35] Laser triangulation : fundamental uncertainty in distance measurement, Rainer G. Dorsch, Gerd Häusler and Jürgen M. Hermann, Applied Optics **33** (1994) 1306–1314.

[36] Active optical feedback in a dual-diode laser configuration applied to displacement measurements with a wide dynamic range, W.M. Wang, K.T.V. Grattan, W.J.O. Boyle and A.W. Palmer, Applied Optics **33** (1994) 1795–1801.

Corner-Cube Retroreflectors

[37] A New Principle in Interferometer Design, E.R. Peck, J.Opt.Soc.Am. **38** (1948) 66.

[38] Theory of the Corner-Cube Interferometer, E.R. Peck, J.Opt.Soc.Am. **38** (1948) 1015–1024.

[39] Polarization Properties of Corner Reflectors and Cavities, E.R. Peck, J.Opt.Soc.Am. **52** (1962) 253–257.

[40] Retroreflecting mirror for dynamic compensation of optical inhomogeneities, V.K. Orlov *et al.*, Sov.J.Quantum Electronics **8** (1978) 799–800.

[41] Retroreflecting arrays as approximate phase conjugators, H.H. Barrett and S.F. Jacobs, Optics Letters **4** (1979) 190–192.

Lasers

[42] Titan-CW Titanium Sapphire Laser, manufacturer's data sheet, Schwartz Electro-Optics (SEO), 3404 N. Orange Blossom Trail, Orlando, FL 32804, USA. Tel. : 407/298-1802. Fax : 298-9889.

[43] Single Frequency Ti:sapphire Laser MBR-110, manufacturer's data sheet, Microlase Optical Systems Ltd., 141 St. James Road, Glasgow G4 OLT, UK. Tel : +44 141 552 8205. Fax : +44 141 552 3906.

[44] Tunable Lasers, manufacturer's data sheet, New Focus, Inc.

[45] Continuously Tunable Diode Lasers, Lasers and Optronics, June 1993.

[46] New dawn beckons for semiconductor lasers, D. Welch, Physics World.

[47] Spectral characteristics of external-cavity controlled semiconductor lasers, Mark W. Fleming and Aram Mooradian, IEEE Journal of Quantum Electronics, Vol. QE-17, No. 1, January 1981, 44–59.

[48] Frequency stabilization of semiconductor lasers by resonant optical feedback, B. Dahmani, L. Hollberg and R. Drullinger, Optics Letters **12** (1987) 876–878.

[49] External-cavity frequency-stabilization of visible and infrared semiconductor lasers for high resolution spectroscopy, M.G. Boshier, D. Berkeland, E.A. Hinds and V. Sandoghdar, Optics Communications **85** (1991) 335–359.

[50] Longitudinal mode control in laser diodes, G.P. Barwood, P. Gill and W.R.C. Rowley, Meas. Sci. Technol. **3** (1992) 406–410.

[51] Self-mixing interference in a diode laser : experimental observations and theoretical analysis, W.M. Wang, W.J.O. Boyle, K.T.V. Grattan and A.W. Palmer, Applied Optics **32** (1993) 1551–1557.

Fibre Optics

[52] High-noise-rejection fibre-optic probe for interferometric applications, M. Martinelli, Optics Letters **7** (1982) 189–191.

[53] Fibre-end interferometric sensor using cooperative retroreflectors, M. Johnson, Optics Letters **8** (1983) 593–595.

[54] Stabilized fibre-end reftroreflecting interferometer, M. Johnson, Applied Optics **23** (1984) 2629–2632.

[55] Remote interferometer using an optical fibre, Toshihiro Kubota, Toshihiko Yoshino and Teruji Ose, Optics Letters **9** (1984) 31–33.

[56] Prefocused optics simplify fiberoptic laser-beam delivery, David Pointer, Laser Focus World, March 1990.

Frequency Measurement

[57] Accurate laser wavelength measurement with a precision two-beam scanning Michelson interferometer, J.-P. Monchalin, M.J. Kelley, J.E. Thomas, N.A. Kumit, A. Szöke, F. Zernike, P.H. Lee and A. Javan, Applied Optics **20** (1981) 736.

[58] Frequency measurements on optically narrowed Rb-stabilised laser diodes at 780 nm and 795 nm, G.P. Barwood, P. Gill, and W.R.C. Rowley, Applied Physics B **53** (1991) 142–147.

[59] The New Wavemeter, Internal Report, The Clarendon Laboratory, Oxford, U.K.

[60] The calibration cavity for Parity Non-Conservation work, Internal Report, The Clarendon Laboratory, Oxford, U.K..

[61] Optically Narrowed Rb-stabilised GaAlAs Diode Laser Frequency Standards with 1.5×10^{-10} Absolute Accuracy, G.P. Barwood, P. Gill and W.R.C. Rowley, SPIE Proceedings **1837** (Frequency-stabilized lasers and their applications), pages 262–70 (1992).

[62] Fringe-counting technique used to lock a suspended interferometer, F. Barone *et al.*, Applied Optics **33** (1994) 1194–1197.

The Phase-Shift Technique

[63] Direct phase detecting system, Y. Ichioka and M. Inuiya, Applied Optics **11** (1972) 1507.

[64] Digital wavefront measuring interferometer for testing optical surfaces and lenses, J.H Bruning *et al.*, Applied Optics **13** (1974) 2693.

[65] Use of an AC heterodyne lateral shear interferometer with real-time wavefront correlation systems, J.C. Wyant, Applied Optics **14** (1975) 2622.

[66] Phase determination of an amplitude modulated complex wavefront, Demetri Psaltis and David Casasent, Applied Optics **17** (1978) 1136.

[67] Optical phase measurement in real time, Lee M. Frantz, Alexander A. Sawchuk and Werner von der Ohe, Applied Optics **18** (1979) 3301.

[68] Chapter 7, The Laser Doppler Technique, L.E. Drain, Wiley (1980).

[69] Digital wave-front measuring interferometry: some systematic error sources, J. Schwider *et al.*, Applied Optics **22** (1983) 3421.

[70] Multichannel phase-shifted interferometer, Osuk Y. Kwon, Optics Letters **9** (1984) 59.

[71] Two-wavelength phase shifting interferometry, Yeou-Yen Cheng and James C. Wyant, Applied Optics **23** (1984) 4539.

[72] Contouring aspheric surfaces using two-wavelength phase-shifting interferometry, Katherine Creath, Yeou-Yen Cheng and James C. Wyant, Optica Acta **32** (1985) 1455.

[73] Computer-aided analysis of holographic interferograms using the phase-shift method, Bernd Breuckmann and Werner Thieme, Applied Optics **24** (1985) 2145.

[74] Phase shifter calibration in phase-shifting interferometry, Yeou-Yen Cheng and James C. Wyant, Applied Optics **24** (1985) 3049.

[75] Phase-shifting speckle interferometry, Katherine Creath, Applied Optics **24** (1985) 3053.

[76] Homogeneity testing by phase sampling interferometry, Johannes Schwider, R. Burow, K.-E. Elssner, R. Spolaczyk and J. Grzanna, Applied Optics **24** (1985) 3059.

[77] Phase-Measurement Interferometry Techniques, Katherine Creath, Progress in Optics XXVI, E. Wolf (1988) 349–393.

[78] pp316–319, Holographic and Speckle Interferometry, 2nd. edition, Robert Jones and Catherine Wykes, Cambridge studies in modern optics: 6, Cambridge University Press (1989), ISBN 0-521-34878-1.

[79] Direct Spatial Reconstruction of Optical Phase from Phase-Modulated Images, Valentin I. Vlad and Daniel Malacara, Progress in Optics XXXIII, E. Wolf (1994) 261–317.

Vibration analysis

[80] Remote vibration measurement of rough surfaces by laser interferometry, Robert A. Bruce and Gerald L. Fitzpatrick, Applied Optics **14** (1975) 1621–1626.

[81] Laser Doppler vibration analysis measuring system using bispectral analysis, Osami Sasaki, Takuso Sato, and Tetsuya Oda, Applied Optics **19** (1980) 151–153.

[82] Method of vibration measurements in heterodyne interferometry, Karl A. Stetson, Optics Letters, **7** (1982) 233–234.

[83] High-speed laser interferometry applied to transient vibration measurements, Richard S. Eng, Kristine A. Langdon, William A. Richardson, and John Lapato, Applied Optics **23** (1984) 2956–2960.

[84] Fringe-counting technique used to lock a suspended interferometer, Fabrizio Barone, Enrico Callone, Rosario De Rosa, Luciano Di Fiore, Francesco Fusco, Leopoldo Milano, and Guido Russo, Applied Optics **33** (1994) 1194–1197.